Active Disturbance Rejection Control for Sensorless PMSM Drive

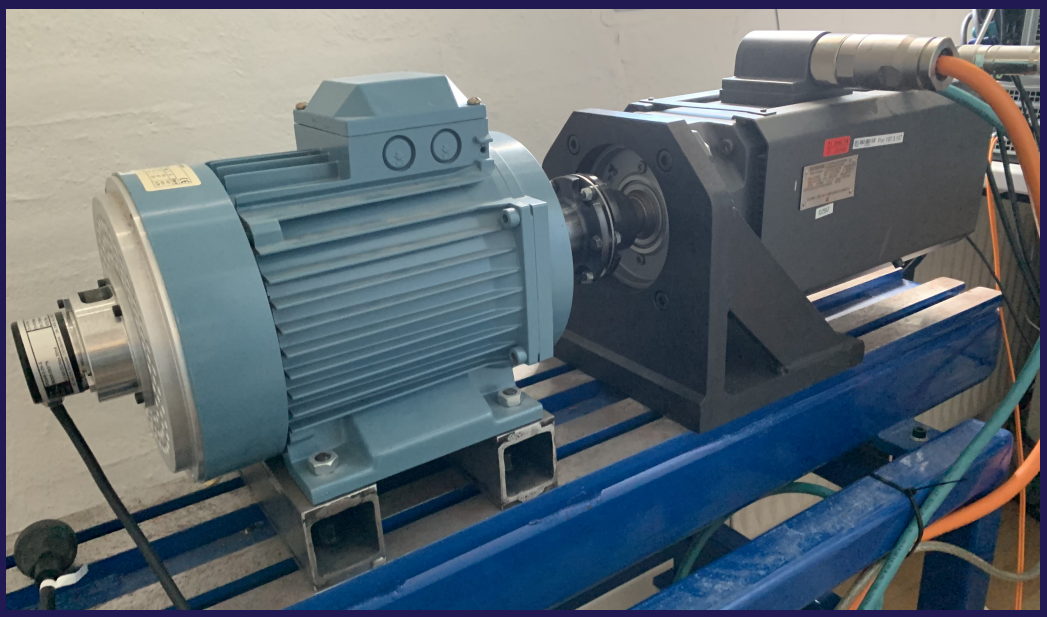

Jakob Blåbjerg Mathiasen

Energy Technology, Group MCE4-1020, 16th of September 2024

Master Thesis

AALBORG UNIVERSITY
STUDENT REPORT

10th Semester
Energy
Pontoppidanstræde 101
9220 Aalborg Øst
http://www.energy.aau.dk

Title:

Active Disturbance Rejection Control for Sensorless PMSM Drive

Project:

Master Thesis

Projectperiod:

2024: May 1st - September 16th

Projectgroup:

MCE4-1020

Participants:

Jakob Blåbjerg Mathiasen

Advisor:

Kaiyuan Lu

Number of pages: 65
Appendix: 8
Finished on: September 16th 2024

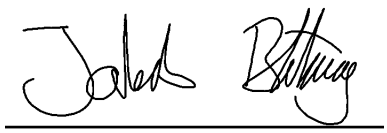

Jakob Blåbjerg Mathiasen

Abstract:

This thesis investigates how a surface mounted permanent magnet synchronous machine (PMSM) performs with an active disturbance rejection controller (ADRC) in both a sensored- and sensorless feedback. The ADRCs are analysed, simulated and experimentally tested and compared to a traditional proportional-integral velocity controller. The sensorless drive is used to estimate the rotor position and it is based on a super twisting algorithm sliding mode observer that estimates the back-EMF of the PMSM. The rotor position is calculated based on the estimated back-EMF and phase locked loops are used to filter the estimated rotor position and estimated velocity of the PMSM. The sensorless drive is implemented into the ADRCs and an analysis is made before testing it in the experimental setup. The analysis investigates how the disturbance rejection properties change as the velocity filter cut-off frequency is lower for the sensorless drive compared to the sensored feedback. It was concluded through experiments and analysis that one of the ADRCs, the phase locked loop observer, had the best performance with both a sensored- and sensorless feedback. When the PMSM was using sensorless feedback it was also concluded the transient performances of the ADRCs had oscillations.

Resumé

Elektriske motorer er brugt i mange applikationer og systemer, som f.eks. elektriske biler, vaskemaskiner og elevatorer. En meget anvendt type af 3-faset elektriskmotorer er permanent magnetiseret synkronmotorer (PMSM), grundet dens høje effektivitet og pålidelighed. Én af styringsmetoderne for en PMSM er feltorienteret kontrol, der benytter sig af kaskadekontrol til at styre såvel motorens mekaniske- og elektriske system. Det mekaniske system styres typisk ved at en hastighedsfejl mellem en reference og målt motor hastighed sendes igennem en proportional-integral (PI) kontroller, som sender en strømreference videre ind i det elektriske system. PI kontrolleren kan være udfordret af pludselig belastningsændringer af motoren, da disse udelukkende kompenseres i forskellen mellem hastighedsreference og målt motorhastighed. PI kontrolstrukturen kan ændres til en aktivforstyrrelsesafvisningskontrol (AFAK), der bruger en forstyrrelsesobservatør til at forudsige, hvor meget ekstra strøm motoren skal bruge for at afvise forstyrrelsen. En AFAK beregner motorens nuværende hastighed på baggrund af strøminput til motoren, og sammenligner den med motorens aktuelle hastighed. Hvis der er en forskel mellem hastigheden af PMSM og den udregnede fra AFAK vil en fase-låst sløjfe beregne forstyrrelsen, og kompensere strøminputtet til at matche hastighedsforskellen. Derfor vil denne afhandling beskæftige sig med, hvordan AFAK kan forbedre en PMSM evne til at kompensere og afvise motorbelastninger.

Feltorienteret kontrol afhænger også af viden om, hvor rotoren af en PMSM er for at kunne skifte mellem referencerammer. Rotorpositionen kan beregnes ved hjælp af en indkoder, men ulempen er, at indkoderen er et ekstra delkomponent der forøger pris, kræver ekstra plads og kan mindske pålideligheden. Et sensorløst drev kan erstatte indkoderen, der ved hjælp af beregningsmetoder og estimeringer kan udregne rotorens position. Positionen kan så bruges til at skifte mellem referencerammerne i feltorienteret kontrol, men også udregne en estimeret hastighed for PMSM, som kan bruges til hastighedsstyring. Positionsestimeringen vil i denne afhandling benytte en glidende tilstands observatør (GTO) til at beregne motorens tilbage elektromotoriske kraft. En ulempe ved at bruge GTO er, at den kan have en svingende opførsel, som kan være beskadigende overfor mekaniske komponenter. Derfor vil rotor positions- og hastighedsestimeringen blive filtreret igennem fase-låste sløjfer.

Denne afhandling vil også kombinere de to metoder, og se hvordan AFAK præstere med et sensorløst drev. For at kunne undersøge disse problemstillinger er der taget udgangspunkt i en forsøgsopstilling med et testmotorsystem, der er koblet sammen til et belastningsmotorsystem. Hele systemet har en indkoder tilkoblet for at bestemme, hvor præcist det sensorløsedrev kan beregne rotorposition af PMSM. For at kunne benytte testopstillingen er testmotorsystemet modelleret, AFAK og sensorløst drev analyseret, tunet og simuleret. AFAK med sensorløst drev er også analyseret igennem blokdiagramsreduktioner, hvor fase-låst sløjfe for hastighed er inkluderet for at se effekten af dens båndbredde i AFAK kontrolstrukturen.
Efter at AFAK er testet både med indkoder og sensorløst drev, kan det konkluderes, at AFAK er bedre til at kompensere belastningsændringer med indkoder og i et sensorløst drev i forhold til PI kontrolleren. Det kan også konkluderes, at det sensorløse drev introducerede svingninger i motorens respons, men tiden fra belastningsændring til stationær tilstand var uændret imellem indkoder- og sensorløst drev.

Preface

This Master Thesis is written by the group MCE4-1020, which is a group on the 4th semester of the Master degree in Mechatronic Control Engineering, at Aalborg University. The thesis was written in the period Mai 2024 to September 2024, and supervised by Kaiyuan Lu.

Reading Guide This thesis is written in LATEX, each chapter is denoted with a certain number, and divided into sections and sub-sections. The appendixes follows the same notation, however with letters. Citations follow the Harvard method. [Surname, year]. A full list of all citations is given in alphabetic order in the bibliography found at the end of the report. The thesis contains 7 chapters, and figures, equation, and tables are numbered by chapter number, thus the first figure in chapter 1 has figure number 1.1 and the subsequent figure has figure number 1.2. Hyperlinks are shown in the PDF version as: Figure 1.1.

The following programs have been used during the writing of this thesis:

- **Overleaf**: For report writing.
- **draw.io**: To construct figures.
- **MATLAB**: For calculation, modelling, data analysis and plots.
- **Simulink**: To simulate responses of presented systems.
- **dSPACE**: For controlling the test setup.

Nomenclature

Abbreviation	Description
ADRC	Active disturbance rejection controller
d-axis	Direct-axis
DC	Direct current
EMF	Electromotive force
ESO	Extended state observer
FOC	Field oriented control
Im	Imaginary axis observer
IM	Induction machine
LPF	Low pass filter
MTPA	Maximum torque per ampere
PI	Proportional-integral
PLL	Phase-locked loop
PLLO	Phase-locked loop observer
PMSM	Permanent magnet synchronous machine
q-axis	Quadrature-axis
RDF	Reference derivative feedforward
Re	Real axis
SMO	Sliding mode observer
STA	Super twisting algorithm
VSI	Voltage source inverter

Greek symbol	Description	Unit
α	α axis	-
β	β axis	-
θ	Angular position	$^\circ \mid rad$
$\hat{\theta}$	Angular position estimation	$^\circ \mid rad$
Δ	Error	-
δ	Noise	-
ζ	damping ratio	
λ	Flux linkage	Wb
ρ	Perturbation term	-
σ	Velocity dependent observer gain	-
τ	Torque	Nm
Φ	Closed loop transfer function	-
ω	Angular velocity | cutoff frequency	rad/s
$\hat{\omega}$	Angular velocity estimation	rad/s
$\dot{\omega}$	Angular acceleration	rad/s^2

Superscript	Description
*	Reference

Symbol	Description	Unit
a	Adjustable parameter	-
A	Equation abbreviation	-
b	Input gain | input coefficient	$\frac{Nm/A}{kg \cdot m^2}$ | -
B	Friction coefficient | equation abbreviation	$Nm \cdot s/rad$ | -
C	Coulomb friction	Nm
d	Disturbance	Nm
$\hat{d}$	Estimated disturbance	Nm
e	Back-EMF | error	V | -
$\dot{e}$	Error derivative	-
$\hat{e}$	Back-EMF estimation	V
f	Function	-
f_s	Sampling frequency	Hz
F	Switching function	-
G	Transfer function	-
h	Observer gain	-
H	Closed loop transfer function PLL	-
i	Current	A
$\hat{i}$	Current estimation	A
$\bar{i}$	Current estimation error	A
J_m	Total rotational inertia	$kg \cdot m^2$
k	Observer gain | Controller gain	- | -
K	Controller gain	-
K_t	Torque constant	Nm/A
L	Inductance	H
N_{PP}	Number pole pairs	-
p	Pole | Natural frequency	- | rad/s
R	Phase resistance	Ω
s	Laplace operator	-
S	Sliding surface | Switch	- | -
t	Time	s
T_d	Digital delay | Total disturbance torque	s | Nm
T_s	Sampling time	s
u	Voltage | input	V | -
V	Lyapunov candidate function	-
$\dot{V}$	Derivative of Lyapunov candidate function	-
w	External disturbances	Nm
x	State	-
$\dot{x}$	State derivative	-
y	Output	-
z	zero	-

Subscripts	**Description**
a	Phase a
b	Phase b
c	Phase c | current | cut-off
c, PLL	Cutoff frequency for PLL
c, pos	Cutoff frequency for position PLL
c, vel	Cutoff frequency for velocity PLL
CL, i	Closed loop current
d	Direct
dq	dq-frame
e	Electrical
est	Estimation
eq	Equivalent
f	Friction
i	Current
is	Integral gain for velocity PI
i, PLL	Integration gain for PLL
i, pos	Integration gain for position PLL
i, vel	Integration gain for velocity PLL
I, i	Integral gain current PI
L	Load
m	Mechanical | Magnetic
mpm	Maximum permanent magnet
o	Observer
obs	Observer
OL, i	Current transfer function open loop
p	Proportional
ps	Proportional gain for velocity loop
p, i	Proportional gain for current PI
p, PLL	Proportional gain for PLL
p, pos	Proportional gain for position PLL
p, vel	Proportional gain for velocity PLL
PLL	Phase-locked loop
q	Quadrature
r	Rotation | Rotor
s	stator | speed | sliding surface
v	Viscous
0	Zero component | velocity working point
$1, 2, ..., \ n$	Iteration number
10	Gain number 1 at velocity working point 0
20	Gain number 2 at velocity working point 0
$, in$	Input to PLL
α	alpha-axis
β	beta-axis

Table of Contents

Introduction 1

The permanent magnet synchronous machine (PMSM) is widely used in industry due to its high efficiency, light weight and high power density [Liang et al., 2017b]. Field oriented control (FOC) is a common control method for the PMSM, which aims to ensure maximum torque per ampere (MTPA) for the PMSM. FOC relies on knowing the rotor position, which often is calculated based on an encoder attached to the PMSM. However the encoder being an extra component that increases cost, weight and potential maintenance many sensorless solutions has been proposed typically based on either back-electromotive force (EMF) estimation or flux observer [Yong et al., 2023]. Back-EMF estimations are based on measurements from the PMSM and motor parameters and thus a sliding mode observer (SMO) can be used to estimate the back-EMF and gain some robustness towards parameter uncertainties within the PMSM [Liang et al., 2017a]. The back-EMF is then used to calculate a rotor position, which is used in the FOC together with an velocity estimation based on the rotor position.
The position- and velocity estimations are used in the FOC control structure, which consists of a cascade structure with an outer velocity loop controlling the velocity reference and an inner current loop that focuses on maintaining MTPA for the PMSM. Proportional-integral (PI) controllers have widely been used for controlling both the velocity- and current loops of the PMSM due to the PI controller's simple structure, high steady state accuracy and high stability, especially, in a linear time-invariant system [Jung et al., 2015]. The PMSM being a non-linear machine, with coupling effects between the inputs and motor parameters changing over time and even during operation [Wilson et al., 2010], means the PMSM is not a linear system. Therefore control methods like active disturbance rejection control (ADRC) [Guo et al., 2017] are used to have better control over the non-linear components of the system and ensure more robust control through the PMSM lifetime. The ADRC also offers good external load rejection, which the PMSM naturally faces as the PMSM has an application where it must perform some kind of task, which includes an external load. The ADRC utilizes an extended state observer (ESO) to estimate the internal and external disturbances [Zuo et al., 2019], which relies on an accurate velocity- and thus accurate position estimation, which with an encoder, is not a challenge. However controlling a PMSM with a sensorless drive put high demand on the position estimation to ensure the performance of the ADRC.

1.1 Active Disturbance Rejection Control

ADRC is possible by transforming a complex system into a cascade of integrators in a canonical form . The cascade of integrators can in general be expressed as in eq. (1.1) on the following page.[Guo et al., 2017]

$$\begin{cases} \dot{x}_1 = x_2 \\ \vdots \\ \dot{x}_{n-1} = x_n \\ \dot{x}_n = f_1(x_1, x_2, \ldots, x_n, w(t), t) + f_0(x_1, x_2, \ldots, x_n) + bu \end{cases} \tag{1.1}$$
$$y = x_1$$

The state variables are given by $x_1, x_2, \cdots x_n$, y is the output, u is the input, b is an input coefficient or gain and $w(t)$ is the external disturbances. The function $f_1(x_1, x_2, \ldots, x_n, w(t), t)$ represents the unknown disturbances in the system and the function $f_0(x_1, x_2, \ldots, x_n)$ represents the known disturbances.
The system being considered a cascade of integrators mean that any change in the states x_n not caused by the input u is considered to be a disturbance to the system. Therefore it is relevant to design some kind of disturbance observer that can compensate the state change not caused by the input u, changes that can be caused either by internal- or external disturbances.
In this thesis different ADRC controllers are designed based on the above general formulation. The ADRC is used in the velocity control loop of the PMSM and their performances are anlysed, simulated and tested experimentally.

1.2 Sensorless Drive

Driving the PMSM with FOC requires knowledge of the rotor position as it is used to change between different references frames that is used to control different parts of a system with a PMSM. The rotor position can be found by using a sensorless drive that uses an observer to estimate the rotor's position based on machine flux or back-EMF, as they have a physical relation to the rotor position [Zuo et al., 2023]. Both methods have its advantageous and suffer from inaccurate estimation at low speeds (<10% rated) due to inverter non-linearity or noise interfering with the signals used for estimating the rotor position [Liang et al., 2017a]. In this thesis a SMO is used to estimate the back-EMF, which then can be used to calculate the rotor position. A filtering method is also needed to ensure the estimated back-EMF and thus rotor position does not contain unwanted high frequency noise, which the nature of SMO introduces. This is done through a phase locked loop (PLL), which has the advantage it also extracts the estimated velocity of the PMSM. The estimated velocity is also filtered to minimize potential noise and ripples in the velocity control. The sensorless schematic can be seen in fig. 1.1.

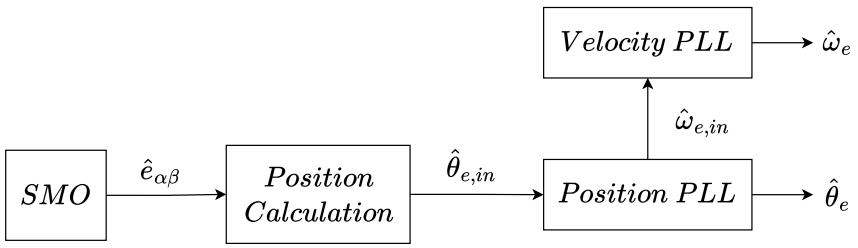

Figure 1.1. *Block diagram of a sensorless drive with position- and velocity processing.*

1.3 Problem Statement

The problem statement with supplementary research questions can be formulated based on the ADRC and sensorless drive mentioned above.

How can a PMSM be controlled with an ADRC in both sensored and sensorless conditions, by using back-EMF to estimate rotor position in the sensorless mode?

- How can ADRC controllers be implemented to improve disturbance rejection properties compared to PI control?
- How can a sensorless drive based on back-EMF estimation and PLL filtering be designed to imitate the encoder feedback PI velocity control performance of the PMSM?
- How does the sensorless drive affect the performance of the ADRC?

1.4 System Description

The experimental setup that is used to investigate the problem statement is drawn in fig. 1.2. The setup consist of a drive system and a load system. The drive system contains of a surface mounted PMSM, a voltage source inverter (VSI) and a dSPACE controller for the motor control. The drive- and load system are connected through a coupling. The load system consists of an induction machine (IM) with an attached encoder to extract the rotor position, VSI and a dSPACE controller. The inverters are supplied by a direct current (DC) power supply.

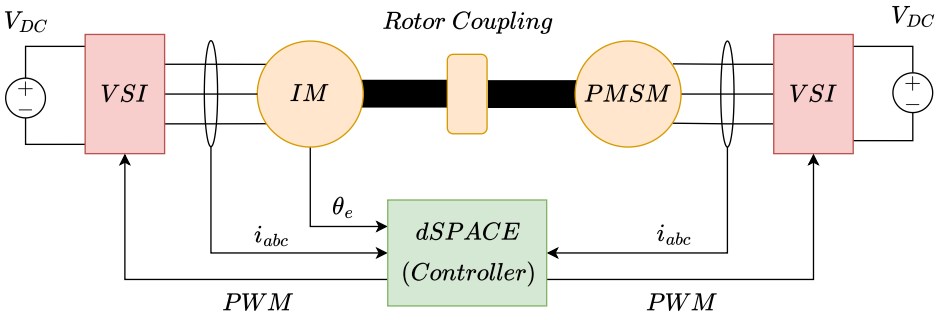

Figure 1.2. *Schematic of the experimental setup.*

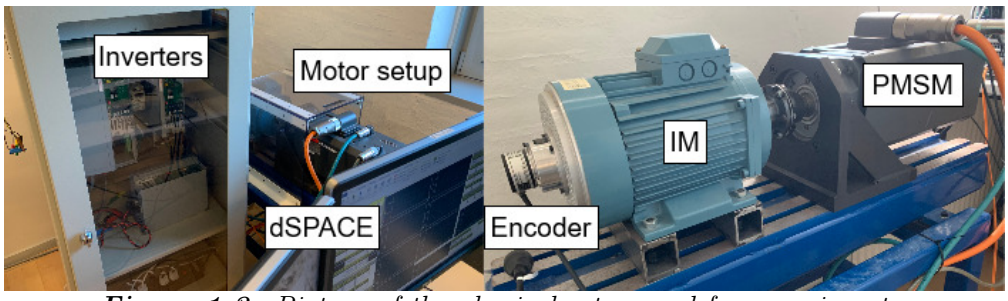

Figure 1.3. *Picture of the physical setup used for experiments.*

The PMSM is a SIEMENS 1FT6084-8SH71-1AA0 [Siemens, 2005] and the IM is an ABB M2AA100LA 3GAA102001-ASA. The IM's motor ratings from the nameplate and the PMSM's parameters and ratings are listed in table 1.1 on the next page. The inverters are danfoss FC302 and the DC-source is 600 V. The encoder is a SCANCON SCA50-2048-D [SCANCON, 2015].

Technical Data	IM	PMSM	Unit
Rated Speed	1430	4500	RPM
Rated torque	14	20	Nm
Rated current	8	24.5	A
Rated voltage	380-420	261	V

PMSM motor parameters			
Symbol	Description	Value	Unit
R	Phase resistance	0.19	Ω
J_m	Total inertia	0.0146	kg/m^2
L_d	Inductance along d-axis	2	mH
L_q	Inductance along q-axis	2	mH
λ_{mpm}	Rotor flux linkage	0.123	Wb
B_v	Viscous friction	0.0014	$Nm\ s/rad$
C	Coulomb friction	0.2429	Nm
N_{pp}	Number of pole pairs	4	-

Table 1.1. *IM- and PMSM motor ratings and PMSM motor parameters.*

The friction parameters are determined experimentally and the test is seen in appendix A on page 60.

1.5 Limitations

In this section the methodology and overall structure of this thesis is described together with limitations and assumptions that are made to limit the scope of the thesis.

Methodology

To solve the problem statement and research questions they are divided into smaller sub-problems and listed below.

Modelling: The PMSM's electrical- and mechanical model are derived based on the stator voltage equations and newtons second law.

Controller design: Based on the PMSM model controllers are designed for the current loops and the velocity loop of the PMSM. An analysis of the ADRC performance is made based on closed-loop transfer functions. The controllers are tested and verified experimentally with encoder feedback. The encoder feedback performance is used as baseline performance.

Sensorless drive: The sensorless drive is derived based on an back-EMF observer that uses SMO. The back-EMF is then used for rotor position- and velocity estimation through PLLs. The sensorless drive is simulated, tested and verified through experiments and compared to the encoder PI velocity control performance.

ADRC with sensorless drive: The ADRC with sensorless feedback is analysed by implementing a velocity PLL into the closed loop transfer functions before it is implemented and tested experimentally.

The simulation- and experimental results are discussed as they are presented through the thesis. Some of the results are further discussed in chapter 6 on page 54, where potential

performance improvements are presented as well.

Limitations

To limit the scope of the thesis a list of limitations and assumptions are made:

- The IM machine's maximum velocity is 1430 RPM, which means the upper velocity of the PMSM is limited to 1400 RPM. The PMSM's rated speed is at 4500 RPM.
- The thesis is not considered with the performance at velocities below 500 RPM.
- The startup method for the sensorless drive is made by utilizing encoder feedback and then switching to the sensorless drive. The startup method and switching instant between encoder- and sensorless feedback is not within the scope of the thesis.
- When the ADRC is running with sensorless feedback it is only considered from the sensorless drive despite the ADRC also provides a possibility of utilizing the velocity estimation within the ESO as feedback.
- The inverter is assumed to be an ideal inverter when being simulated.
- It is assumed the IM is capable of providing an ideal step when it is modelled in simulations.
- The experiments are only made in the positive rotation direction of the PMSM.

Model 2

In this chapter a model of the PMSM is made. The model consists of an electrical machine model, which is derived in the $\alpha\beta$- and dq-reference frame, and a mechanical model that is based on Newton's second law. The PMSM is controlled by FOC and the inner current loops are designed and tested in this chapter. The outer velocity loop is controlled by PI and ADRCs and they are designed and tested in chapter 3 on page 15.

2.1 Reference Frames

The PMSM is modelled in different reference frames due to each reference frame has different advantageous over the other. In this thesis the abc-, $\alpha\beta$- and dq-reference frames are used and they are illustrated in fig. 2.1.

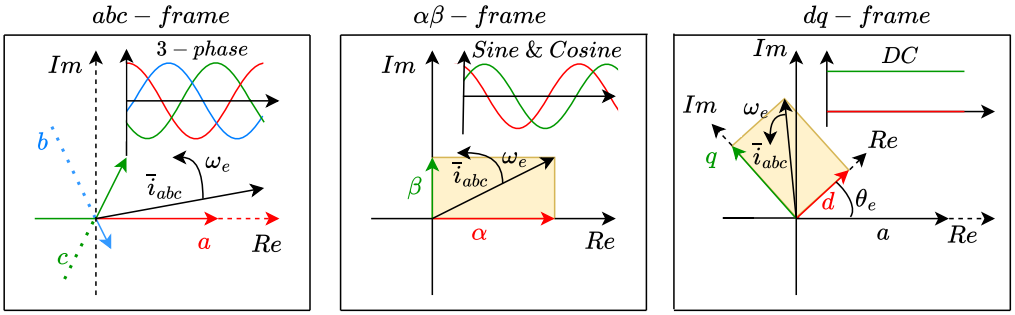

Figure 2.1. *abc-, αβ- and dq-reference frames.*

The PMSM uses three phase currents to run and the stationary abc-frame represents the actual current that is sent to the PMSM. The $\alpha\beta$-reference frame is also stationary and represents the real and imaginary parts of a space vector. The real part α is placed directly on the electrical phase a and the imaginary component β is placed perpendicular to α on the imaginary axis. The $\alpha\beta$-reference frame is used to control the gate signals of the inverter and for rotor position estimation in the sensorless control. The dq-frame is a rotating reference frame, which means the steady state signals appears as DC-signals. This makes the dq-frame a suitable frame when modelling and controlling the PMSM.

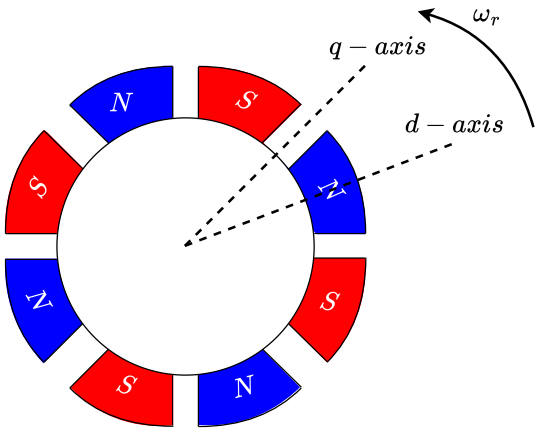

Figure 2.2. *dq-axis placement in the PMSM.*

The d-axis is placed on a north pole of the rotor, where ω_r is the rotational direction, as seen in fig. 2.2, and the q-axis is leading the d-axis by 90° electrical degrees. Producing current on the q-axis creates a magnetic field that provide torque to the PMSM. The PMSM has four pole pairs and this means that one mechanical rotation, $\omega_m(t)$, is equal to four electrical rotations, $\omega_e(t)$, as in eq. (2.1), where N_{pp} is the number of pole pairs.

$$\omega_m(t) = \omega_e(t) \cdot N_{pp} \tag{2.1}$$

The permanent magnets of the PMSM are surface mounted. This makes the PMSM non-salient due to the uniform reluctance, where the permanent magnets can be seen as an air gab due to the low permeability of the magnet, which is close to the permeability of air [Fitzgerald and Kingsley, 2014]. The inductance can then be assumed to be the same in all direction and thus the d- and q-inductance are equal.

$$L_d = L_q = L_s \tag{2.2}$$

Stator Voltage Equations

To rotate the rotor of the PMSM currents flow through the stator windings and create a rotating magnetic field. The stator can be described through an electrical circuit in the dq-reference frame and it is illustrated in fig. 2.3 on the following page. The electrical circuits consists of two RL circuits with dependent voltage sources that represent the back-EMF coupling between the dq-axis, which changes with the motor velocity. The equations that describe the circuits in fig. 2.3 on the next page is refered to as the stator voltage equations.

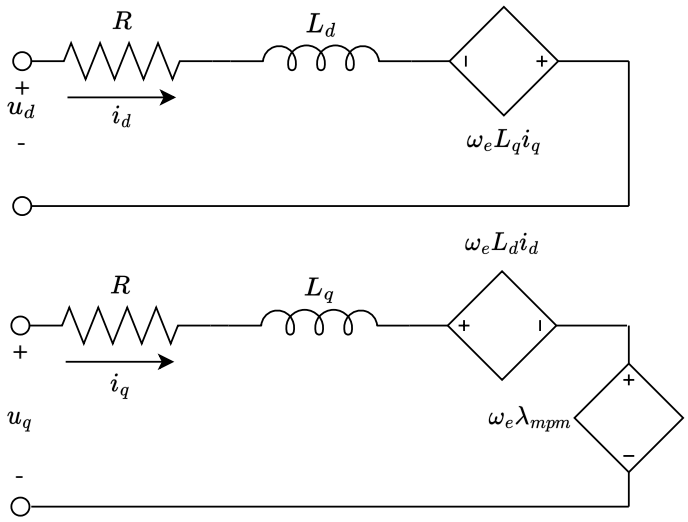

Figure 2.3. *Equivalent electrical circuit of PMSM in dq-frame.*

The inputs to the circuits are the voltages $u_d(t)$ and $u_q(t)$, which causes the $i_d(t)$ and $i_q(t)$ currents to run through the circuits. The resistance, R, is the stator phase winding resistance, L_d and L_q are the inductances related to the flux along the d- and q-axis. $\omega_e(t)$ is the electrical angular velocity and the flux linkage of the permanent magnets of the rotor is denoted λ_{mpm}. The stator voltage equations is then given by eq. (2.3) based on the electrical circuits in fig. 2.3.

$$\begin{aligned} u_d(t) &= Ri_d(t) + \frac{d}{dt}\lambda_d(t) - \omega_e(t)\lambda_q(t), \qquad \lambda_d(t) = L_d i_d(t) + \lambda_{mpm} \\ u_q(t) &= Ri_q(t) + \frac{d}{dt}\lambda_q(t) + \omega_e(t)\lambda_d(t), \qquad \lambda_q(t) = L_q i_q(t) \end{aligned} \tag{2.3}$$

The voltage equations in eq. (2.3) can be further reduced from the assumption of non-saliency changing L_d and L_q into an equivalent L_s. Inserting the flux linkage expressions of $\lambda_d(t)$, $\lambda_q(t)$ and combine the back-EMF terms to $e_d(t)$ and $e_q(t)$ results in an expression for the stator voltage equation as in eq. (2.4).

$$\begin{aligned} u_d(t) &= Ri_d(t) + \frac{d}{dt}i_d(t)L_s + e_d(t), \qquad e_d(t) = -\omega_e(t)L_s i_q(t) \\ u_q(t) &= Ri_q(t) + \frac{d}{dt}i_q(t)L_s + e_q(t), \qquad e_q(t) = \omega_e(t)(L_s i_d(t) + \lambda_{mpm}) \end{aligned} \tag{2.4}$$

The current dynamics of eq. (2.4) can then be isolated by rearranging the equations as in eq. (2.5). The current dynamics are later used to design current controllers for the current loop of the PMSM.

$$\begin{aligned} \frac{d}{dt}i_d(t) &= \frac{1}{L_s}(u_d(t) - Ri_d(t) - e_d(t)) \\ \frac{d}{dt}i_q(t) &= \frac{1}{L_s}(u_q(t) - Ri_q(t) - e_q(t)) \end{aligned} \tag{2.5}$$

Stator Voltage Equations in $\alpha\beta$-frame

The stator voltage equation can also be described through the stationary $\alpha\beta$-frame. This becomes useful when designing a sensorless drive for the PMSM to estimate the rotor

position. A transformation matrix can be used to transform the rotating dq-frame into the stationary $\alpha\beta$-frame as in eq. (2.6).

$$\begin{bmatrix} f_\alpha \\ f_\beta \\ f_0 \end{bmatrix} = \underbrace{\begin{bmatrix} cos(\theta_e(t)) & -sin(\theta_e(t)) & 0 \\ sin(\theta_e(t)) & cos(\theta_e(t)) & 0 \\ 0 & 0 & 1 \end{bmatrix}}_{Transformation\ matrix} \begin{bmatrix} f_d \\ f_q \\ f_0 \end{bmatrix} \tag{2.6}$$

To apply this transformation the rotor position $\theta_e(t)$ is required. The stator voltage equations in eq. (2.4) on the preceding page can be rewritten into vector form as in eq. (2.7). The system is assumed to be balanced and thus the zero-component is left out.

$$\begin{bmatrix} u_d(t) \\ u_q(t) \end{bmatrix} = \begin{bmatrix} R + \frac{d}{dt}L_s & -\omega_e(t)L_s \\ \omega_e(t)L_s & R + \frac{d}{dt}L_s \end{bmatrix} \cdot \begin{bmatrix} i_d(t) \\ i_q(t) \end{bmatrix} + \begin{bmatrix} 0 \\ \omega_e(t) \cdot \lambda_{mpm} \end{bmatrix} \tag{2.7}$$

Applying the transformation matrix from dq- to $\alpha\beta$-frame eq. (2.6) gives the stator voltage equation in the $\alpha\beta$-frame as in eq. (2.8).

$$\begin{aligned} u_\alpha(t) &= Ri_\alpha(t) + \frac{d}{dt}i_\alpha(t)L_s + e_\alpha(t), & e_\alpha(t) &= -\omega_e(t) \cdot \lambda_{mpm} \cdot sin(\theta_e(t)) \\ u_\beta(t) &= Ri_\beta(t) + \frac{d}{dt}i_\beta(t)L_s + e_\beta(t), & e_\beta(t) &= \omega_e(t) \cdot \lambda_{mpm} \cdot cos(\theta_e(t)) \end{aligned} \tag{2.8}$$

Rearranging the equations and isolating for the current dynamics results in eq. (2.9) and is later used when designing the sensorless drive for the PMSM.

$$\begin{aligned} \frac{d}{dt}i_\alpha(t) &= \frac{1}{L_s}(u_\alpha(t) - Ri_\alpha(t) - e_\alpha(t)) \\ \frac{d}{dt}i_\beta(t) &= \frac{1}{L_s}(u_\beta(t) - Ri_\beta(t) - e_\beta(t)) \end{aligned} \tag{2.9}$$

2.2 The Mechanical Model

The mechanical model is considering the PMSM's mechanical forces, which includes the PMSM itself, the coupling and the IM. The PMSM's equation of motion is described by Newtons's second law and is seen in eq. (2.10).

$$J_m\dot{\omega}_m(t) = \tau_e(t) - \tau_f(t) - \tau_L(t) \tag{2.10}$$

J_m is a representation of the total inertia in the system, which includes the individual inertias of the PMSM, IM and coupling. The acceleration is denoted as $\dot{\omega}_m(t)$ and $\tau_e(t)$ is the electrical torque. $\tau_f(t)$ is the friction torque and $\tau_L(t)$ is the load torque from the IM.

The electrical torque $\tau_e(t)$ is the input to the system and the general torque equation for a three phase AC machine is seen in 1) at eq. (2.11) on the next page. The torque generated is dependent on the number of pole pairs, the currents and magnetic fluxes in the dq-frame. Inserting the magnetic fluxes in eq. (2.3) on the facing page into the

equation results in 2), and applying the non-saliency inductance relation results in the final torque expression of the PMSM in 3), where K_t is the torque constant.

$$\begin{aligned} &1) \quad \tau_e(t) = \frac{3}{2}\, N_{pp}\, (\lambda_d(t) i_q(t) - \lambda_q(t) i_d(t)) \\ &2) \quad \tau_e(t) = \frac{3}{2}\, N_{pp}\, (L_d i_q(t) i_d(t) + \lambda_{mpm} i_q(t) - L_q i_q(t) i_d(t)) \\ &3) \quad \tau_e(t) = \frac{3}{2}\, N_{pp}\, \lambda_{mpm}\, i_q(t) = K_t i_q(t) \end{aligned} \tag{2.11}$$

The friction term is non-linear and it is assumed to consists of a static coulomb term C and a viscous friction term B_v that is linear dependent with the velocity $\omega_m(t)$ and expressed as in eq. (2.12).

$$\tau_f(t) = B_v \omega_m(t) + C sign(\omega_m(t)) \tag{2.12}$$

The coulomb friction is used as current off-set when comparing simulations with the experiments, and is not used for controller design. This is due to the non-linear behavior around zero with the *sign* function and due to the drive cycle in this thesis only being in the positive rotational direction and when the PMSM is already at a running speed.

Inserting the expressions of the friction- and input torque into eq. (2.10) on the preceding page results in an equation of motion of the system, where the static Coulomb friction C is disregarded.

$$J_m \dot{\omega}_m(t) = \frac{3}{2}\, N_{pp}\, \lambda_{mpm}\, i_q(t) - B_v \omega_m(t) - \tau_L(t) \tag{2.13}$$

The load $\tau_L(t)$ is an unknown input to the model from the IM. This means it is considered as an external disturbance into the system and is not described through any other expression than τ_L.

2.3 FOC and Current Controller Design

FOC is a cascade control structure that consist of an outer velocity loop and an inner current loop for the PMSM and can be seen in fig. 2.4 on the next page. The FOC uses the *dq*-reference frame for controlling the torque input to the PMSM. The velocity error between the velocity reference $\omega_m^*(t)$ and the measured velocity $\omega_m(t)$ goes through the ADRC controller and results in the current reference for the q-axis $i_q^*(t)$. To generate MTPA the FOC aims to maintain the d-axis current at zero and provide all the current to the q-axis. The output of the *dq*-current PI controllers are the voltage references $v_{dq}^*(t)$, that is transformed into the $\alpha\beta$-frame. The voltage references, $v_{\alpha\beta}^*(t)$, are used to do space vector pulse width modulation (SVPWM) for controlling the VSI. The amount of torque that is sent to the PMSM depends on changes in reference velocity, $\omega_m^*(t)$ and incoming disturbances to the system.

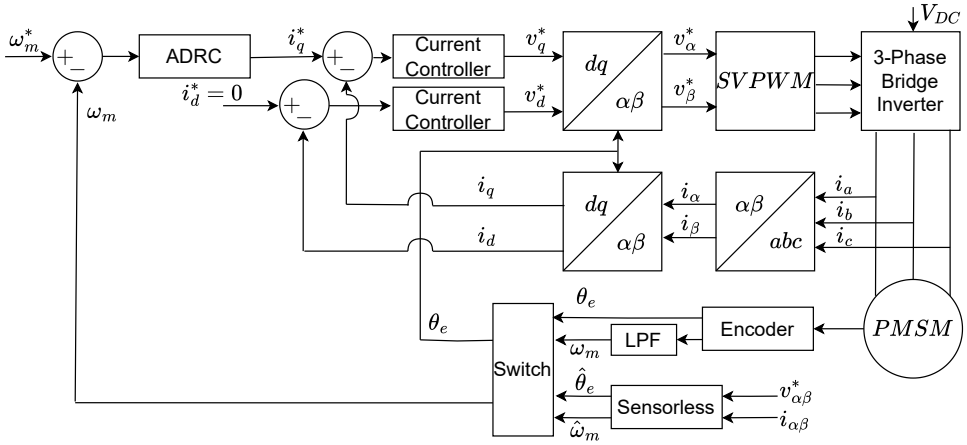

Figure 2.4. *Field oriented control block diagram.*

The rotor position and PMSM velocity can be calculated by an encoder or estimated through an observer, which can be seen by the inputs to the switch block in fig. 2.4. The encoder calculation of the velocity being a derivative of the position means the signal contains noise, which is compensated through a low pass filter (LPF).

Current Controller

The inner current loops PI controllers are designed from the current dynamic equations in eq. (2.5) on page 8. The PMSM being non-salient results in both current controllers have the same motor parameters and dynamics. This means Laplace transforming the current dynamics for $\frac{i_d(s)}{v_d(s)}$ and consider the back-EMF as a disturbance results in the open-loop transfer function in eq. (2.14), which is similar for $\frac{i_q(s)}{v_q(s)}$.

$$\frac{i_d(s)}{v_d(s)} = \frac{1}{L_s s + R} \tag{2.14}$$

This results in a first order transfer function with a pole placed at $s = -\frac{R}{L_s}$. As the transfer function for $\frac{i_q(s)}{v_q(s)}$ is identical to eq. (2.14) only one controller needs to be designed and will be used for both current controllers.

Digital compensation for the back-EMF is also commonly used to decouple the back-EMF when the PMSM is running [Li et al., 2023]. This relies on accurate motor parameters and velocity measurements. When the velocity is measured by the encoder the back-EMF compensation may improve the performance but it is not necessary the case for a sensorless drive that estimates the velocity. If the velocity estimation is inaccurate or contains noise this could potentially lead to a back-EMF compensation that degrades the PMSM performance. Therefore a digital back-EMF compensation is not used in this thesis, and to verify the designed current controller a test is made where the motor is at standstill and thus no back-EMF is present.

Ideally a controller would take a measurement, do the control calculation and send an output instantaneously. However there is a calculation delay that needs to be considered and it is assumed that it is a maximum of one and half the sampling time of the system. The digital delay can be modelled as in eq. (2.15) on the following page, where the digital

delay is $T_d = T_s \cdot 1.5$ and the sampling time is given as $T_s = \frac{1}{f_s}$. The switching frequency is $f_s = 5\ kHz$, and from eq. (2.15) it can be seen the pole of the digital delay is placed at $s = -\frac{1}{T_d}$.

$$G_d(s) = \frac{1}{T_d \cdot s + 1} \tag{2.15}$$

The current loop is illustrated in fig. 2.5, and if the closed-loop system is tuned such that the calculation delay pole is significantly faster than the current loop, it can be neglected.

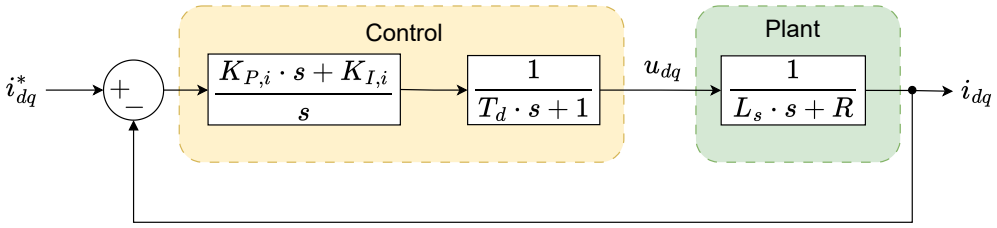

Figure 2.5. *Block diagram of current loop.*

The PI controller contains a zero and a free integrator. The zero is used for pole-zero cancellation of the system pole located at $s = -\frac{R}{L_s}$. The free integrator is placed to ensure fast response, and the PI gains can be determined analytically. The open-loop transfer function of the current loop in fig. 2.5 is given in eq. (2.16), where the digital delay is neglected.

$$G_{OL}(s) = \frac{K_{P,i}s + K_{I,i}}{s} \cdot \frac{1}{L_s s + R} = \frac{K_{P,i}s + K_{I,i}}{s(L_s s + R)} \tag{2.16}$$

The closed-loop transfer function with unity feedback is then given by eq. (2.17)

$$G_{CL}(s) = \frac{G_{OL}(s)}{1 + G_{OL}(s)} = \frac{K_{P,i}s + K_{I,i}}{L_s s^2 + (R + K_{P,i})s + K_{I,i})} \tag{2.17}$$

The poles and zero of the closed-loop system can then analytical be determined. This is done by taking the numerator equal to zero and solving for s. Similar approach for the denominator, but since the denominator is a second order equation the quadratic formula is used and the results are seen in eq. (2.18) and (2.19).

$$z_{CL,i} = -\frac{K_{I,i}}{K_{P,i}} \tag{2.18}$$

$$p_{CL,i} = -\frac{R + K_{P,i} \pm \sqrt{-4L_s K_{I,i} + K_{P,i}^2 + 2RK_{P,i} + R^2}}{2L_s} \tag{2.19}$$

Now these two equations can be used to make an expression for the parameters $K_{P,i}$ and $K_{I,i}$ being a function of $z_{CL,i}$ and $p_{CL,i}$. First the positive part of eq. (2.19) is solved with respect to $K_{P,i}$.

$$K_{P,i} = -\frac{L_s p_{cl,i}^2 + R p_{cl,i} + K_{I,i}}{p_{cl,i}} \tag{2.20}$$

Then finding an expression for $K_{I,i}$ in eq. (2.18) on the facing page, inserting it into eq. (2.20) on the preceding page and solving for $K_{P,i}$ results in eq. (2.21). This expression of $K_{P,i}$ is dependent on choosing a desired position of the closed-loop- zero and pole.

$$K_{P,i} = -\frac{p_{CL,i} \cdot (R + L_s \cdot p_{CL,i})}{p_{CL,i} - z_{CL,i}} \tag{2.21}$$

An expression for $K_{I,i}$ can similarly be found from eq. (2.20) on the preceding page. Now an expression for $K_{P,i}$ is found from eq. (2.18) on the facing page and inserted into eq. (2.20) on the preceding page and solved with relation to $K_{I,i}$. This results in an expression for $K_{I,i}$ in eq. (2.22).

$$K_{I,i} = -\frac{z_{CL,i} \cdot p_{CL,i} \cdot (R + L_s \cdot p_{CL,i})}{p_{CL,i} - z_{CL,i}} \tag{2.22}$$

The PI gains can now be determined based on the placement of the closed-loop- pole and zero. Placing the zero at $z_{CL,i} = -\frac{R}{L_s}$ and placing the pole at $-1200\ \frac{rad}{s}$ gives a fast response where the calculation delay can be neglected. The PI parameters are then $K_{P,i} = 2.4$ and $K_{I,i} = 228$ and are tested in lab to validate the performance.

Closed inner loop test

The inner current loop is tested by closing the loop and give a current step input on the d-axis. Providing current to the d-axis amplifies the magnetic field of the permanent magnets, but does not produce any torque to the PMSM. This means the PMSM is at standstill and that the coupled back-EMF terms are neglectable in the test. The test is made by stepping the current from 5 A to 7 A, which minimizes the inverter non-linearities that is caused by the diode voltage drop. The result of the test can be seen in fig. 2.6.

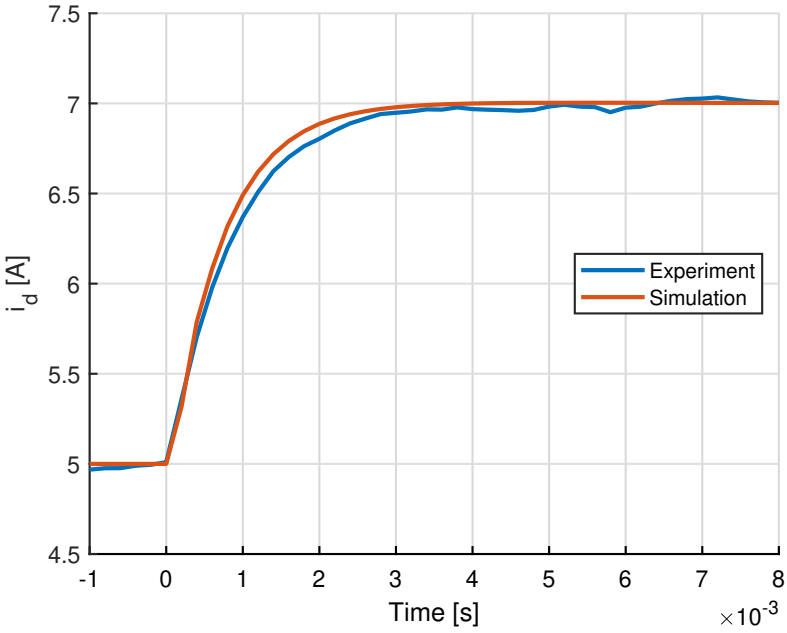

Figure 2.6. *Step response of i_d current.*

The current step shows that the experimental setup has a slightly slower rise time and settling time compared to the simulation. This indicates the parameters of R and L_s have some deviations or there is some unmodelled inverter dynamics, which is not compensated for by stepping from 5 A to 7 A. The performance deviations are minimal and therefore the designed current controllers are used in the experimental setup.

Through this chapter the PMSM has been modelled by the stator voltage equations and Newtons second law. The stator voltage equations has been established in the dq- and $\alpha\beta$-reference frames and the FOC block diagram has been presented. The inner current loop has also been designed and validated experimentally. The outer velocity loop has not been designed in this chapter but will be analysed and tuned in the following chapter.

Active Disturbance Rejection Control 3

In this chapter the ADRC in the speed loop is designed and is based on [Zuo et al., 2019]. Two different variations of a disturbance observer that observes changes between the input acceleration and the measured velocity is presented, tested with an encoder feedback and compared to conventional velocity PI controller. Before testing the performance of the ADRCs an analysis are made for the load rejection and noise attenuation with an encoder feedback.

3.1 Design of ADRC

The ADRC is based on the PMSM's equation of motion, which is restated in eq. (3.1). The equation can be reformulated as in eq. (3.2), where $T_d(t)$ is the total disturbance torque, and consists of $T_d(t) = K_t(i_q^*(t) - i_q(t)) + \tau_L(t) + B_v\omega_m(t)$, where K_t is the torque constant, i_q^* is the q-axis current reference, τ_L is the load torque and B_v the viscous friction. Then in eq. (3.3) the input gain b and total disturbance $d(t)$ is formed by dividing by the moment of inertia J_m.

$$J_m\dot{\omega}_m(t) = K_t i_q(t) - B_v\omega_m(t) - \tau_L(t) \tag{3.1}$$

$$\dot{\omega}_m(t) = \frac{K_t}{J_m}i_q^*(t) - \frac{T_d(t)}{J_m} \tag{3.2}$$

$$\dot{\omega}_m(t) = bi_q^*(t) + d(t) \tag{3.3}$$

The total disturbance term $d(t)$ both includes internal and external disturbances such as parameter deviations, friction and load changes, whereas traditional PI only treats the external load as a disturbance. The tracking error can be expressed as $e_s(t) = \omega_m^*(t) - \omega_m(t)$, where $\omega_m^*(t)$ is the mechanical reference velocity, and it can be linked to the equation of motion in eq. (3.3) as in eq. (3.4).

$$\dot{e}_s(t) = \dot{\omega}_m^*(t) - \dot{\omega}_m(t) = \dot{\omega}_m^*(t) - bi_q^*(t) - d(t) \tag{3.4}$$

The velocity control law is given in eq. (3.5) and results in a first-order error dynamics, where k_{ps} is the proportional gain on the speed error.

$$\dot{e}_s(t) = -k_{ps}e_s(t) \tag{3.5}$$

Now inserting the error terms $\dot{e}_s(t)$ and $e_s(t)$ into eq. (3.5) and isolating for the control gain $bi_q^*(t)$ results in eq. (3.6) on the next page.

$$bi_q^*(t) = \dot{\omega}_m^*(t) + k_{ps}(\omega_m^*(t) - \omega_m(t)) - d(t) \tag{3.6}$$

In this expression of the control law in eq. (3.6) the derivative of the reference $\dot{\omega}_m^*(t)$ is called the reference derivative feedforward (RDF). This term does not influence the disturbance rejection properties and is therefore excluded from the control law expression. The total disturbance $d(t)$ is the unknown disturbance in the system and thus it cannot be a part of the control law. Instead it is replaced with an estimation called $d_{est}(t)$, which is to be estimated by an observer. The mechanical velocity is obtained either through the derivative of the encoder or from the velocity estimation in the sensorless control. Either methods could introduce noise into the system and the total noise is defined as $\delta(t)$, and thus the output is defined as in eq. (3.7).

$$y(t) = \omega_m(t) + \delta(t) \tag{3.7}$$

The output $y(t)$ containing the noise term $\delta(t)$ means a filtering method needs to be used before calculating the velocity error in the control system to avoid chattering or instability due to noise. The encoder feedback is denoted $\omega_m(t)$ and the sensorless feedback is denoted $\hat{\omega}_m(t)$. Excluding the RDF, inserting the estimated disturbance and using encoder feedback results in a final expression of the control law as in eq. (3.8).

$$i_q^*(t) = \frac{k_{ps}(\omega_m^*(t) - \omega_m(t)) - d_{est}(t)}{b} \tag{3.8}$$

The control law states that there are two factors that causes the controller to change its output. The first one being changing the velocity reference, and the second having a change in the estimated disturbance $d_{est}(t)$. A block diagram of the control law with a disturbance observer- and velocity extraction block, which represents either sensorless or encoder feedback, can be seen in fig. 3.1.

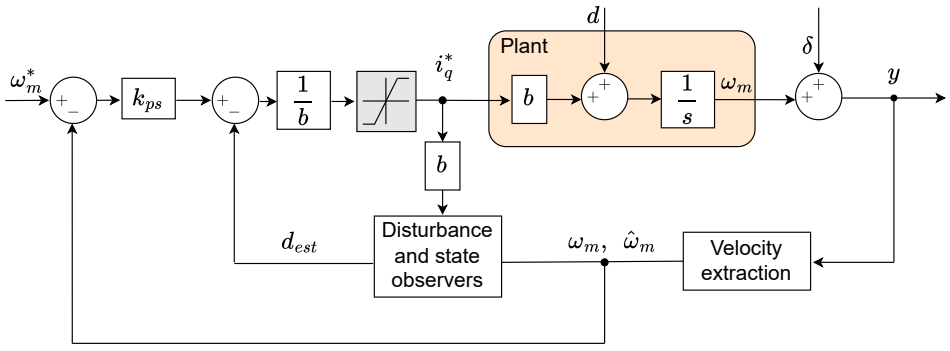

Figure 3.1. *Block diagram of the control law with a disturbance observer.*

In fig. 3.1 there is implemented a saturation for safety when testing the controller in lab, but is not included in the controller analysis. The signal output $y(t)$ is both used as the velocity- and ADRC feedback.

3.2 Disturbance Observer

To investigate the dynamics of the ADRC a method for estimating the disturbance, $d_{est}(t)$, must be established together with closed-loop frequency response analysis. In

this thesis the disturbance observer is an acceleration observer based on [Zuo et al., 2019], that estimates the disturbance $d_{est}(t)$.

The traditional PI velocity controller reacts on a load disturbance by measuring the velocity drop and compensates the velocity error through the velocity loop. The acceleration observer is made from having an error signal between the measured output $y(t)$ and estimated observer velocity $\omega_{obs}(t)$, which is estimated based on a PLL structure as seen in the green part of the block diagram in fig. 3.2. The observer velocity $\omega_{obs}(t)$ is found by the observer acceleration $\dot{\omega}_{obs}(t)$, which is estimated from the sum of the input torque $bi_q^*(t)$ and estimated disturbance $d_{est}(t)$, which is the output of the observer PI in the yellow part of fig. 3.2. Acceleration being of higher order than velocity should result in a faster disturbance rejection compared to the traditional PI control.

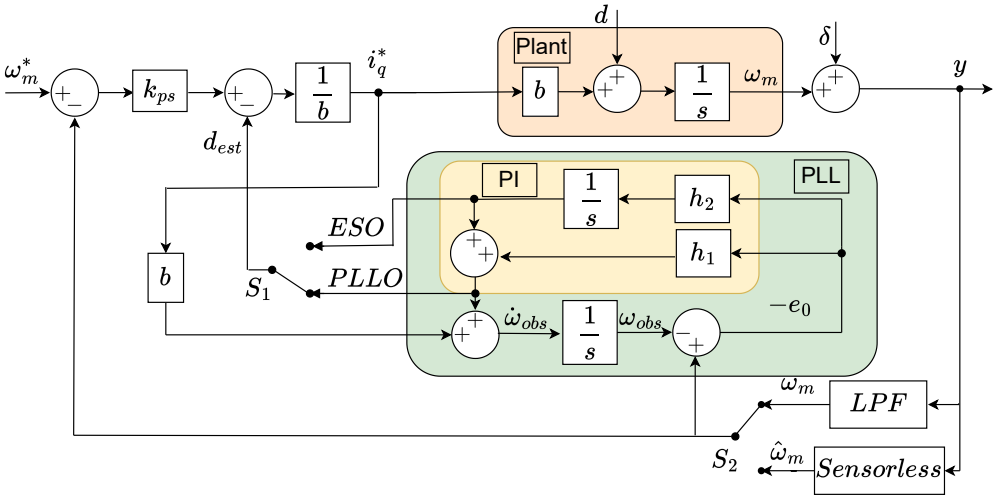

Figure 3.2. *Disturbance observer block diagram.*

The error signal $e_0(t)$ of the velocities is sent to the observer PI that estimates the disturbance $d(t)$ using an approximation of eq. (3.9). The approximation is seen in eq. (3.10) and $d_{est}(t)$ is the part of the estimated acceleration $\dot{\omega}_{obs}(t)$ not caused by the reference acceleration $bi_q^*(t)$.

$$\dot{\omega}_m(t) = bi_q^*(t) + d(t) \tag{3.9}$$

$$\dot{\omega}_{est}(t) = bi_q^*(t) + d_{est}(t) \tag{3.10}$$

The disturbance observer itself has a PLL structure and assuming no noise the acceleration observer ensures that the velocity error $e_0(t)$ is driven to zero and the estimated disturbance $d_{est}(t) = d(t)$ in steady state. The estimated disturbance $d_{est}(t)$ is also used in the control law of eq. (3.6) on the preceding page, and $d_{est}(t)$ can either be chosen as the output of the yellow PI sum in fig. 3.2 of the observer or the PI integrator. This is illustrated by the switch, S_1 in fig. 3.2 and the output of the observer PI integrator is denoted ESO and the output of the PI observer is denoted PLLO. The observer velocity $\omega_{obs}(t)$ could also be used as velocity feedback in the outer velocity loop, but as stated in the limitation section in section 1.5 on page 5 the ADRC will either be using encoder- or sensorless feedback. The use of either encoder- of sensorless feedback is illustrated by the switch S_2 in the block diagram. The ESO and $PLLO$

controllers are analyzed and their performances are both tested using encoder feedback and later in chapter 5 on page 43 with sensorless feedback. A traditional PI controller is also developed and illustrated in fig. 3.3 and its performance is similarly compared to the *PLLO* and *ESO*.

3.3 Closed-Loop Analysis

Closed-loop responses are derived for the *PI* controller and ADRCs to have a better understanding of their dynamics. In the block diagram fig. 3.2 on the previous page it can be seen that there are three inputs, $\omega_m^*(t)$, $d(t)$ and $\delta(t)$ and one plant output $\omega_m(t)$. The full closed loop response can be expressed as a sum of closed loop responses as expressed in eq. (3.11), where the closed loop responses are denoted with Φ and a subscript for each of the inputs.

$$\omega_m(s) = \Phi_{\omega_m}(s)\omega_m^*(s) + \Phi_d(s)d(s) + \Phi_\delta(s)\delta(s) \tag{3.11}$$

To analyse each of the closed-loop responses of eq. (3.11) it is assumed two of the three inputs are kept at zero while deriving a closed-loop transfer function for the third input. The derivations of the closed-loop transfer functions of all the ADRCs can be found in appendix B on page 61.

PI Controller

The traditional *PI* controller estimates the disturbance by integrating the speed error. The block diagram of the *PI* controller can be seen in fig. 3.3, where it is assumed the current controllers closed loop response are without influence on the velocity loop.

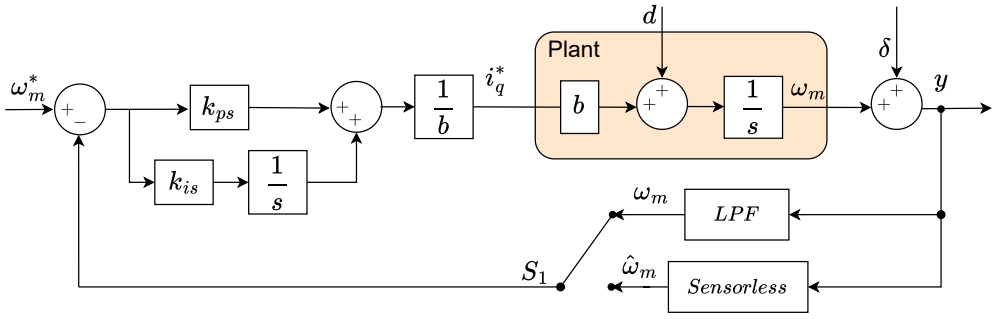

Figure 3.3. *Traditional PI controller.*

The *PI* controller closed-loop transfer functions of the velocity reference, disturbance and noise can be seen in eq. (3.12), (3.13) and (3.14). The transfer functions are analysed together with the ESO and PLL in section 3.5 on page 21 and section 3.6 on page 23.

$$\Phi_{\omega_m}(s) = \frac{\omega_m(s)}{\omega_m^*(s)} = \frac{k_{ps}s + k_{is}}{s^2 + k_{ps}s + k_{is}} \tag{3.12}$$

$$\Phi_d(s) = \frac{\omega_m(s)}{d(s)} = \frac{s}{s^2 + k_{ps}s + k_{is}} \tag{3.13}$$

$$\Phi_\delta(s) = \frac{\omega_m(s)}{\delta(s)} = -\frac{k_{ps}s + k_{is}}{s^2 + k_{ps}s + k_{is}} \tag{3.14}$$

Acceleration Observer

The switch, S_1, in fig. 3.2 on page 17 can either be connected to the ESO or PLLO. Switching between the ESO and PLLO changes the closed-loop responses of the disturbance $\frac{\omega_m(s)}{d(s)}$ and the noise $\frac{\omega_m(s)}{\delta(s)}$. The closed-loop response of the reference velocity $\frac{\omega_m(s)}{\omega_m^*(s)}$ does however not change when assuming the disturbance and noise is zero, when deriving the closed-loop responses. The closed-loop reference velocity $\frac{\omega_m}{\omega_m^*}(s)$ can be seen in eq. (3.15) and is derived in appendix B on page 61.

$$\frac{\omega_m(s)}{\omega_m^*(s)} = \frac{k_{ps}}{s + k_{ps}} \tag{3.15}$$

The closed-loop velocity reference is a first-order transfer function, that only depends on the velocity gain k_{ps}.

Extended State Observer

Connecting the switch S_1 to the ESO signal in fig. 3.2 on page 17 results in an ESO constructed for eq. (3.3) on page 15 in eq. (3.16), (3.17) and (3.18).

$$e_0(s) = \omega_{obs}(s) - y(s) \tag{3.16}$$

$$s\omega_{obs}(s) = bi_q^*(s) + d_{est}(s) - h_1 e_0(s) \tag{3.17}$$

$$d_{est}(s) = -\frac{1}{s} h_2 e_0(s) \tag{3.18}$$

The velocity error $e_0(s)$ is defined as the error between the observer's estimated velocity $\omega_{obs}(s)$ and the output $y(s)$. The gains h_1 and h_2 are the observer gains. Assuming zero input for $\omega_m^*(s)$ and $\delta(s)$, the disturbance closed-loop transfer function of the ESO can be derived and is seen in eq. (3.19). the derivation can be found in appendix B on page 64.

$$\Phi_d(s) = \frac{\omega_m(s)}{d(s)} = \frac{s(s + h_1)}{(s + k_{ps})(s^2 + h_1 s + h_2)} \tag{3.19}$$

The noise closed-loop transfer function is derived by assuming $d = 0$ and $\omega_m^* = 0$ and the noise δ is the input. The derivation can be found in appendix B on page 65 and the noise closed-loop transfer function for the ESO is then given by eq. (3.20).

$$\Phi_\delta(s) = \frac{\omega_m(s)}{\delta(s)} = \frac{s^2(s + h_1)}{(s + k_{ps})(s^2 + h_1 s + h_2)} - 1 \tag{3.20}$$

Phase Locked Loop Observer

Connecting the switch S_1 in fig. 3.2 on page 17 to $PLLO$ results in observer equations that is slightly modified from the ESO as seen in eq. (3.21) on the following page, (3.22) and (3.23).

$$e_0(s) = \omega_{obs}(s) - y(s) \tag{3.21}$$

$$s\omega_{obs}(s) = bi_q^*(s) + d_{est}(s) \tag{3.22}$$

$$d_{est}(s) = -h_1 e_0(s) - \frac{1}{s} h_2 e_0(s) \tag{3.23}$$

The difference between the ESO and PLLO is the estimated disturbance $d_{est}(s)$ used for load compensation. The PLLO uses the observer PI sum of $e_0(s)$, which modifies the disturbance rejection and noise attenuation. The closed-loop disturbance- and noise transfer function can be seen in eq. (3.24) and eq. (3.25). The derivation is in appendix B on page 61.

$$\Phi_d(s) = \frac{\omega_m(s)}{d(s)} = \frac{s^2}{(s + k_{ps})(s^2 + h_1 s + h_2)} \tag{3.24}$$

$$\Phi_\delta(s) = \frac{\omega_m(s)}{\delta(s)} = \frac{s^3}{(s + k_{ps})(s^2 + h_1 s + h_2)} - 1 \tag{3.25}$$

The difference between connecting to either the ESO or $PLLO$ is that the ESO only uses the integration term of the observer PI. The dynamics of a PI controller being the integrator eliminates steady state error over time and the proportional term reacting fast to changes means the ESO only utilizes the slower responding integration term. The $PLLO$ on the other hand also uses the faster proportional term h_1, which means the load change are faster rejected, which is also seen in the closed-loop transfer function zeros. The $PLLO$ has a double zero at the imaginary axis, whereas the $PLLO$ has one zero at the imaginary axis and the other is placed at $s = -h_1$. The trade off is then that the proportional term h_1 also increases noise in the disturbance rejection whereas the integration term is better at noise attenuation.

3.4 Controller Parameters

The different parameters of k_{ps}, k_{is}, h_1 and h_2 must be tuned to have comparability between the performances of the PI, ESO and PLLO controllers. It is possible to minimize the amount of tuneable parameters to three by having a closer look at the second order system in the denominator of the PLLO and ESO. By choosing the damping of the second order system to be $\zeta = 1$ the natural frequency p_0 can determine the gains of h_1 and h_2 directly from eq. (3.26).

$$s^2 + h_1 s + h_2 = s^2 + 2\zeta p_0 s + p_0^2 \tag{3.26}$$

$$h1 = 2p_0 \tag{3.27}$$

$$h2 = p_0^2 \tag{3.28}$$

This results in the observer being a critically damped second-order system with the natural frequency p_o.

The disturbance- and noise closed-loop transfer functions for the $PLLO$ and ESO have both k_{ps} and p_0 in the denominator. However the transfer function of tracking $\frac{\omega_m(s)}{\omega_m^*(s)}$ in eq. (3.15) on page 19 is only dependent on k_{ps}, which means that tuning p_0 can be done without influencing the closed-loop tracking transfer function. However changing k_{ps} results in the dynamics of tracking, disturbance and noise to be changed as k_{ps} is present in all closed loop transfer function denominators for the ADRCs. Similarly does the traditional PI controller have parameter dependency for tracking, disturbance rejection and noise attenuation as k_{ps} and k_{is} are present in all the transfer functions in section 3.3 on page 18.

The parameter dependency of k_{ps} between $PLLO$, ESO and PI results in finding optimal gains for each controller are more complex. To have some comparability between the PI, ESO and $PLLO$ the k_{ps} gain is the same for all three controllers. This leaves k_{is} and p_0 as the two control parameters that are independent of each other. With k_{ps} being fixed between the controllers means p_0 only influences the noise attenuation and disturbance rejection of the $PLLO$ and ESO. The k_{is} on the other hand influences performances of the tracking, disturbance and noise of the PI, as it is in all the denominators in (3.12)-eq. (3.14) on page 18. Therefore it is decided that the controllers must be able to settle within 0.5 s when a velocity reference is given a step change.

Based on these criteria the controller parameters are suggested to be $k_{ps} = 40\frac{rad}{s}$, $p_0 = 20\frac{rad}{s}$ and $k_{is} = k_{ps} \cdot 5 = 200\frac{rad}{s}$ and listed in table 3.1. The integrator gain k_{is} is multiplied by 5, which by simulation shows the PI controller analytically is capable of settling withing 0.5 s when the reference velocity is changed. The natural frequency p_0 of the observer gains h_1 and h_2 are iteratively determined to be placed at $p_0 = 20\frac{rad}{s}$.

Parameter	k_{ps}	p_0	k_{is}
Value	40	20	200

Table 3.1. *Controller parameters.*

3.5 Disturbance Rejection Analysis

The closed-loop transfer functions of the disturbance for the different controllers can be seen in eq. (3.29)

$$\Phi_d(s) = \begin{cases} \dfrac{s}{s^2 + k_{ps}s + k_{is}} & \text{PI} \\ \dfrac{s(s+h_1)}{(s+k_{ps})(s^2+h_1s+h_2)} & ESO \\ \dfrac{s^2}{(s+k_{ps})(s^2+h_1s+h_2)} & PLLO \end{cases} \tag{3.29}$$

Bode plots are made of the three closed-loop transfer functions to analyse the disturbance rejection. The parameters inserted into the closed-loop transfer functions are those described in the previous section. The bode plots can be seen in fig. 3.4 on the following page.

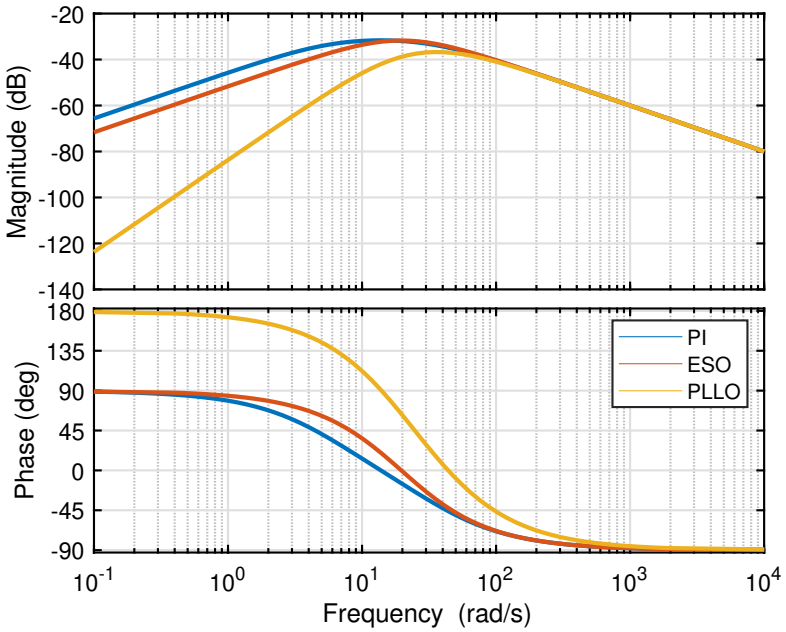

Figure 3.4. *Bode plot of the disturbance closed-loop transfer functions.*

The bode plots illustrate that the $PLLO$ has the best load rejection in the low-frequency range. This is due to the $PLLO$ has a double zero placed at the imaginary axis, which gives magnitude slope of 40 $\frac{dB}{dec}$ in the low-frequency range. The PI and ESO have a slope of 20 $\frac{dB}{dec}$ and thus a similar load rejection, where the placement of k_{is} and p_0 determines which controller has a better disturbance rejection. It is also expected that the peak value, and thus velocity drop, is lowest for the $PLLO$ when a load change occurs. This is due to the $PLLO$ has the least peak value in the bode plot compared to the ESO and PI. Since the actual disturbance in the system is unknown the phase shift is not relevant as it is a measure of the phase shift between the input and output of the transfer function.

In the experimental setup a load torque change is applied by the IM machine. It is assumed the IM is capable of performing an ideal step change of the load. Therefore the disturbance closed-loop transfer functions in eq. (3.29) on the previous page are given a unity step input to see how they perform before testing it in the real setup. The unity step responses are illustrated in fig. 3.5 on the facing page.

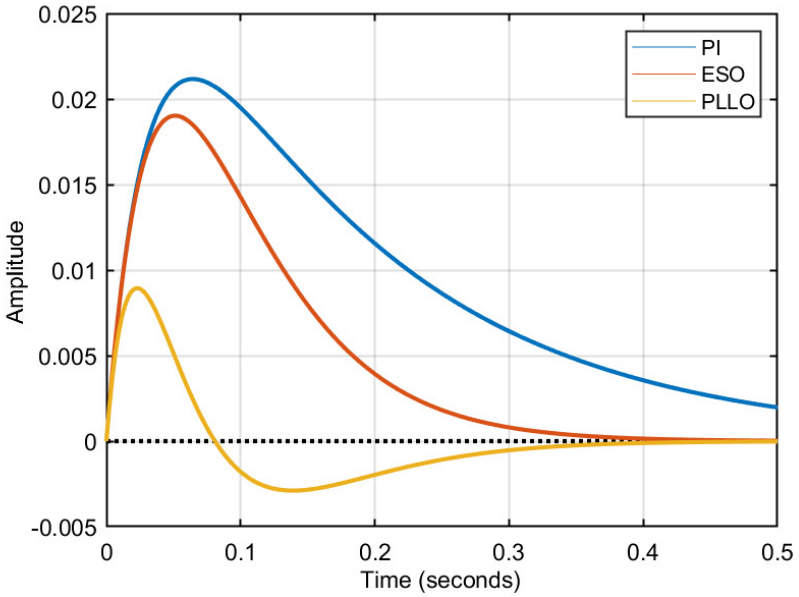

Figure 3.5. *Step response of the disturbance closed-loop transfer functions.*

The step responses illustrates that for the chosen controller parameters the $PLLO$ has the fastest change of current due to the smallest amplitude change. The settling times of the $PLLO$ and ESO are similar, which arises from having the same poles and placement in the characteristic equation of the closed-loop transfer function. The transients however differ, which is a consequence of the estimated disturbance $d_{est}(s)$ in eq. (3.18) on page 19 and eq. (3.23) on page 20 either contains the proportional gain from h_1 in the observer or not. The ESO and PI controller both have load rejection response without overshooting the velocity reference, where the ESO has a better load rejection compared to the PI due to the pole placement of the controllers. The $PLLO$ overshoots the reference as the unity disturbance input is rejected, despite being tuned with a natural damping of $\zeta = 1$. Comparing the ESO and $PLLO$ transfer functions in eq. (3.29) on page 21, the only difference between them is the placement of the zeros in the numerator. This means the double zero at the imaginary axis for the $PLLO$ results in the load rejection of the $PLLO$ being faster with smaller amplitude compared to the ESO, but also with a reference overshoot as the load is rejected.

3.6 Noise Rejection Analysis

The closed-loop transfer functions of the noise for the different controllers can be seen in eq. (3.30). The parameters are the same as in table 3.1 on page 21 and the bode plots can be seen in fig. 3.6 on the following page.

$$\Phi_\delta(s) = \begin{cases} -\dfrac{k_{ps} + k_{is}}{s^2 + k_{ps}s + k_{is}} & \text{PI} \\ \dfrac{s^2(s + h_1)}{(s + k_{ps})(s^2 + h_1 s + h_2)} - 1 & ESO \\ \dfrac{s^3}{(s + k_{ps})(s^2 + h_1 s + h_2)} - 1 & PLLO \end{cases} \tag{3.30}$$

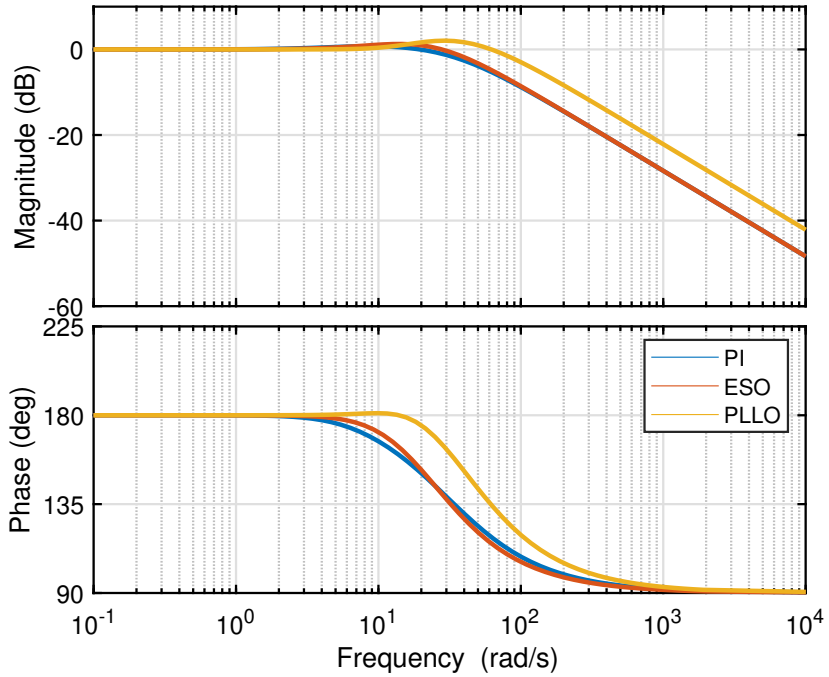

Figure 3.6. *Bode plot of the noise closed-loop transfer functions.*

The bode plots illustrate that the noise attenuation are similar in the low-range frequencies, and the gain decreases with 20 $\frac{dB}{dec}$ in the high-frequency range. The cut-off frequencies of the three controllers differ, and the PLLO passes more frequencies than the ESO and PI controller. The noise attenuation is dependent on the pole placement and there is then a trade-off between disturbance rejection performance and noise attenuation. In the experiment it is not expected that noise has a large impact when using encoder feedback, due to the laboratory setup is isolated against EMI. However when running with a sensorless configuration it is expected that the noise can be a limiting factor due to the sensorless drive using a SMO that by nature causes chattering. This is further described and analysed in chapter 4 on page 29 and chapter 5 on page 43.

The PI, ESO and PLLO controllers are tested with an encoder feedback to compare their performances and evaluate the analysis results with the experiments.

3.7 Encoder Feedback ADRC

The drivecycle in the experiment are illustrated in fig. 3.7 on the next page and consists of tests with and without load. The PMSM starts with a no-load ramp of the reference velocity from 500 RPM to 1200 RPM. The reason for using a ramp instead of a step is to avoid saturation for large reference changes and to better compare the response when doing sensorless experiments. Then a step load change is made at $t = 2s$ of 5 Nm in the opposing rotating direction slowing the PMSM down. Then the load is released at $t = 3s$ and at $t = 4s$ the PMSM is slowed down from 1200 RPM to 1000 RPM. A no-load sinusoidal velocity reference is then given $\pm$ 400 RPM at $t = 5s$ and finally a $\pm$ 10 Nm sinusoidal load change is given at $t = 7s$. In the ADRC block diagram in fig. 3.2 on page 17 it can be seen that there is a LPF after the velocity calculation from the encoder and the cut-off frequency is 100 Hz.

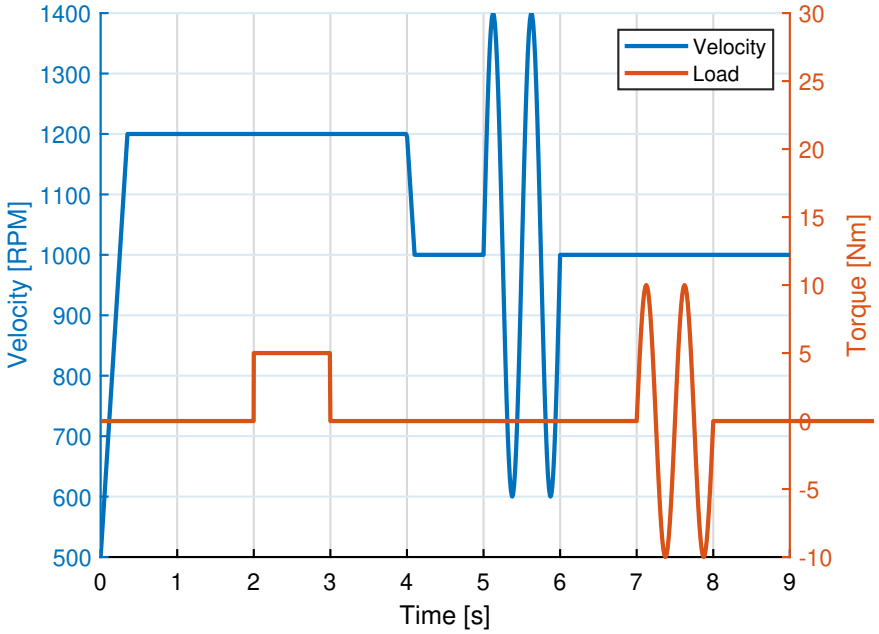

Figure 3.7. *PMSM drive cycle to test no-load and load responses.*

The tests with encoder feedback can be seen in fig. 3.8 with a zoom on the ramp transients, in fig. 3.9 on the following page is a closer look at the load changes and in fig. 3.10 on page 27 is the sinus performances visualized. The gains used for the PI, $PLLO$ and ESO are the same as in table 3.1 on page 21.

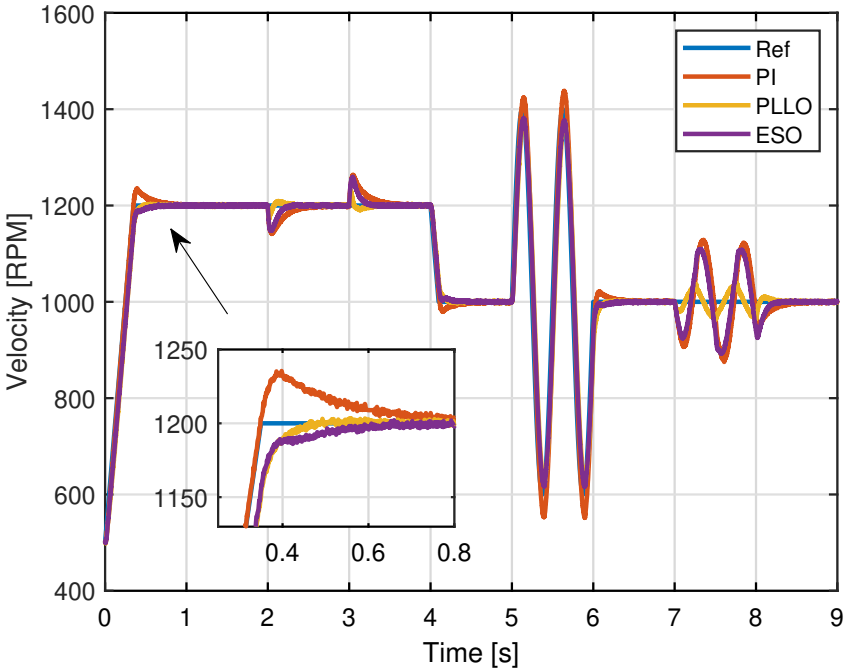

Figure 3.8. *Velocity response of the drivecycle with encoder feedback.*

The experiments show that at the different stages of the drive cycle the controllers performances varies. The PI controller is better at following the ramp reference compared to the $PLLO$ and ESO controllers. This is due to the integrator being able to adjust for the speed error, and making the PI controller a second order system, which can follow ramp inputs with no steady state error. As seen in eq. (3.15) on page 19 the ESO and $PLLO$ controllers have a first order dynamic for the reference velocity and therefore an

error will occur as long as the ramp input continuous. The velocity error can be minimized if the controller gain k_{ps} is increased. When the reference is met at 1200 RPM the PI controller overshoots whereas the $PLLO$ and ESO maintains their first order response and settles faster than the PI controller. The ESO and $PLLO$ do not have the same transient response despite having the same closed-loop transfer function at no-load. This could be caused by parameter uncertainties, which is faster compensated in the $PLLO$ controller compared to the ESO controller. Parameter uncertainty causes the input gain b to either be too large or small compared to the ideal value. This means that having too large an input gain b results in an overshoot whereas too small a value would result in an underdamped system, which also seems to be the case for the ESO. In fig. 3.9 is a zoomed view of the load changes of 5 Nm starting at $t = 2$ s.

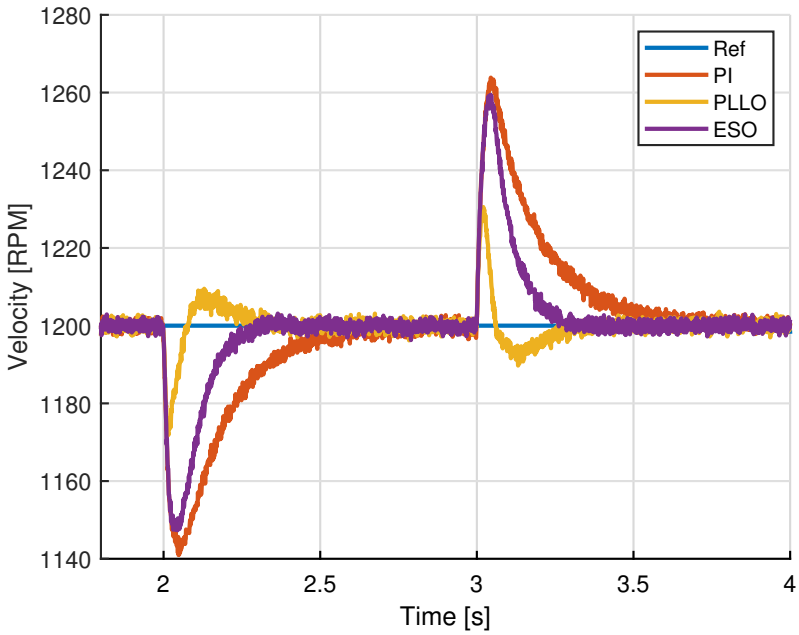

Figure 3.9. *Load step responses of 5 Nm at $t = 2$ s in the drivecycle.*

When the load is changed it can be seen in fig. 3.9 that the $PLLO$ has the fastest load rejection and settling time compared to the ESO and PI. This is supported by the disturbance rejection analysis from the previous section as well as the ESO has a faster load rejection compared to the PI controller. After the 5 Nm load is rejected and the PMSM is running at steady state at $t = 2.5$ s there are no obvious steady state ripple differences between the controllers. This indicates the noise within the system is filtered away by the encoder LPF filter. In fig. 3.10 on the facing page there is a graph highlighting the sinusoidal velocity- and load references in the drivecycle.

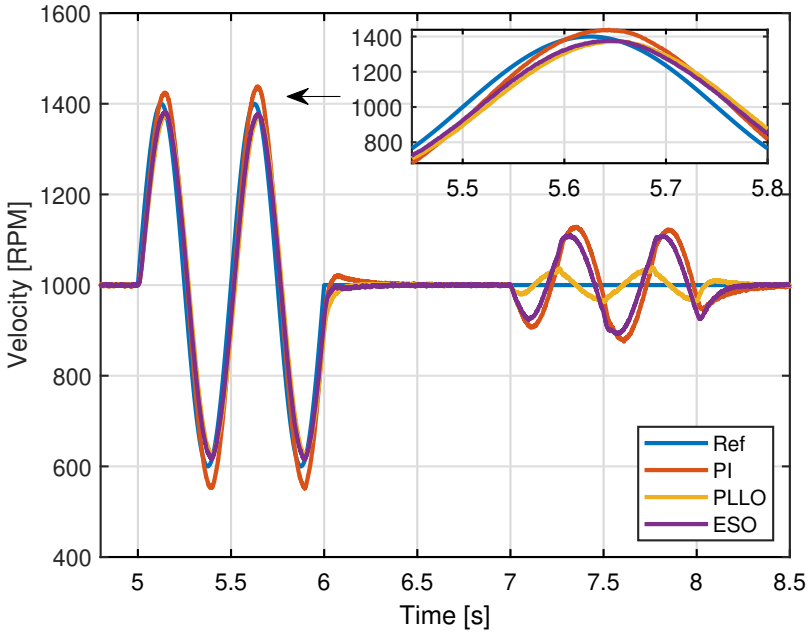

Figure 3.10. *Current response of the drivecycle with encoder feedback.*

The no-load sinus reference input illustrates that the controllers almost have similar tracking performances. The controllers are not able to follow the sinus reference without tracking error due to the input frequency of the sinus is 2 Hz. The reference tracking pole, eq. (3.15) on page 19, of ESO and $PLLO$ are determined by k_{ps} and is placed at $40\frac{rad}{s}$. This means it is faster than 2 Hz but if it were plotted in a bode diagram it would be clear that the magnitude has a negative amplification at 2 Hz. This means k_{ps} should be retuned in order to be even faster than the frequency of the sinus input to minimize the sinus reference error. However this would of course change the dynamics of the disturbance rejection and noise attenuation as well. The PI is also not fast enough to follow the sinus reference and it has an overshoot at the peak sinus reference, whereas the $PLLO$ and ESO are lagging the reference and does not meet the peak reference of the sinus. Assuming the pole of the ADRCs are fast enough to track the sinus reference, the input gain b would also play a role for the $PLLO$ and ESO, where too high a value results in an under damped response and a too low input gain would result in an over damped response.

The sinus load performances at $t = 7$ s also illustrates how the load rejection properties behave of the controllers. Again the $PLLO$ has a faster load rejection of the 10 Nm sinus load, and when the peak velocity drop occurs for the ESO and PI controller at ie. $t = 7.25$ s the $PLLO$ has returned to the reference velocity. This is due to the disturbance input is at 2 Hz, which based on the analysis made in fig. 3.4 on page 22 showed the disturbance rejection of the $PLLO$ is within the region of $40\frac{dB}{dec}$ decrease for the $PLLO$ compared to the decrease of $20\frac{dB}{dec}$ for the PI and ESO controllers. This means the magnitude of of the $PLLO$ in the bode plot in fig. 3.4 on page 22 is lower compared to the ESO and PI, thus better load rejection as seen in the experiment. The ESO is also better at rejecting the load compared to the PI, which can be seen by the ESO having lower peak values and faster change of velocity as the load is rejected. This is also supported by the bode plot in fig. 3.4 on page 22, where the magnitude of the ESO is lower at 2 Hz compared to the PI, which is verified in the experiment.

3.8 Summery of ADRC

Through this chapter ADRCs have been derived, analyzed and tested in simulations and experiments. Disturbance analysis and experimental tests have shown the $PLLO$ provides the best disturbance rejection compared to the ESO and PI controllers. The ESO also rejects disturbances faster than the traditional PI controller with the used controller parameters. The controller parameters are tuned by having the same velocity error gain k_{ps} and letting the disturbance observer gains k_{is}, h_1 and h_2 being tuneable. Through the experiments it was also clear that noise was not of importance with encoder feedback as the controller performances were comparable to the analytical performance. In the following chapter a sensorless control method is derived for the PMSM, which is later implemented together with the ADRC controllers.

Sensorless Control 4

This chapter derives a sensorless control structure for the PMSM. The position estimation is based on a super twisting algoritmh (STA) SMO, that estimates the back-emf of the PMSM. The back-EMF is used to calculate the rotor position, which is filtered through a PLL. The rotor position PLL also extracts a velocity estimation, which is filtered through a velocity PLL. The sensorless drive is then simulated, tested and validated experimentally with the PI velocity controller. In chapter 5 on page 43 the sensorless control is connected to the ADRC and an analysis is made before implementing it into the PMSM.

4.1 Rotor Position Estimation

FOC relies on knowing the position of the PMSM's rotor. This can be done in various ways, but there are two common methods for extracting the rotor position, which is either using the back-EMF or magnetic flux $\lambda_m(t)$ of the PMSM. In fig. 4.1 a phasor diagram illustrates the placement of the magnetic flux $\lambda_m(t)$ the back-EMF $e_{\alpha\beta}(t)$ together with the stator voltage equation in eq. (2.8) on page 9 in relation to the $\alpha\beta$- and dq- axis. [Zuo et al., 2023]

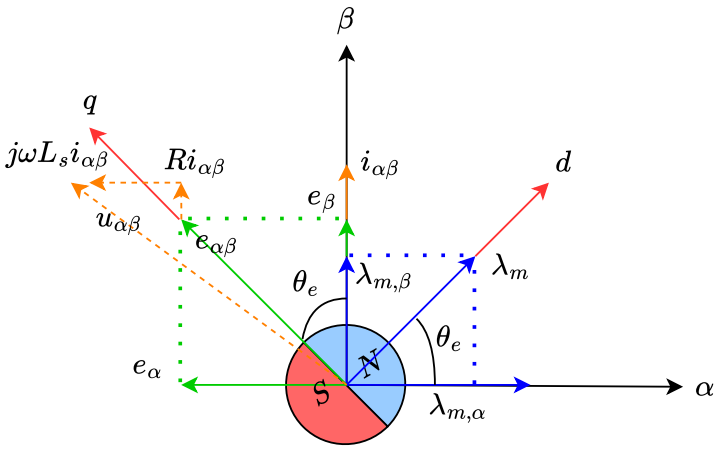

Figure 4.1. *Illustration of λ_m and $e_{\alpha\beta}$ in relation to the dq- and $\alpha\beta$-axis.*

The magnetic flux $\lambda_m(t)$ is aligned with the d-axis of the rotor. The back-EMF is the derivative of the magnetic flux $\lambda_m(t)$ and displaced with 90° aligning it with the q-axis. The back-EMF $e_{\alpha\beta}(t)$ is a space vector, and using the $\alpha\beta$ components of the back-EMF the angle of the space vector can be calculated as in eq. (4.1).

$$\theta_e(t) = tan^{-1}(\frac{-e_\alpha(t)}{e_\beta(t)}) = tan^{-1}(\frac{\lambda_{m,\beta}(t) - L_s \cdot i_\beta(t)}{\lambda_{m,\alpha}(t) - L_s \cdot i_\alpha(t)}) \tag{4.1}$$

If the estimation of the position is too inaccurate there is a risk of the system becoming unstable. In fig. 4.2 it can be seen, that an inaccurate position estimation leads to the placement of the d- and q-axis currents being displaced in relation to the actual rotor. As FOC tries to maintain the d-axis current at zero an inaccurate position estimation will contribute to generate d-axis current, which can be seen in eq. (4.2) and eq. (4.3).

$$i_d(t) = \hat{i}_d(t) \cdot cos(\hat{\theta}_e(t)) + \hat{i}_q(t) \cdot sin(\hat{\theta}_e(t)) \tag{4.2}$$

$$i_q(t) = \hat{i}_d(t) \cdot sin(\hat{\theta}_e(t)) + \hat{i}_q(t) \cdot cos(\hat{\theta}_e(t)) \tag{4.3}$$

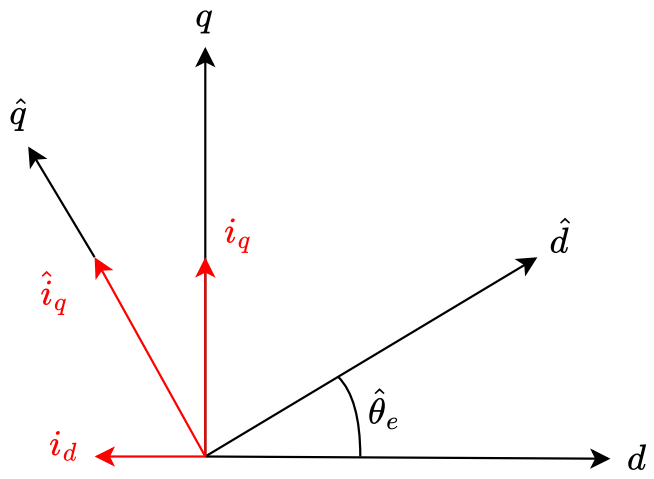

Figure 4.2. *Estimation error of $\hat{\theta}_e$ results in displacement of $\hat{i}_q$.*

To gain further insight into how the stability of the system can be effected the error term is inserted into Newton's second law equation eq. (2.10) on page 9 and becomes eq. (4.4).

$$\dot{\omega}_m(t) = \frac{1}{J_m}(K_t \cdot \hat{i}_q(t) \cdot cos(\hat{\theta}_e(t)) - \tau_f(\hat{\omega_m}, t) - \tau_L(t)) \tag{4.4}$$

The motor torque is reduced with $cos(\hat{\theta}_e(t))$, which means that the higher the position estimation error is the smaller is the torque generation of the PMSM. This could potentially lead to motor stop if the torque generation is not enough to overcome the other terms of eq. (4.4).

Likewise an inaccurate position estimation would lead to an inaccurate velocity estimation that could degrade the performance of the ADRC. The ADRC uses the measured motor velocity to do load compensation, and as the sensorless drive estimates the velocity based on the position estimation, inaccuracies might degrade the ADRC's load rejection performance. The control law in eq. (3.8) on page 16 is rewritten in eq. (4.5) to illustrate the state estimation inaccuracies that might occur, as $\hat{d}_{est}$ is dependent on both $\hat{i}_q^*(t)$ and $\hat{\omega}_m(t)$.

$$\hat{i}_q^*(t) = \frac{k_{ps}(\omega_m^*(t) - \hat{\omega}_m(t)) - \hat{d}_{est}(\hat{i}_q^*(t), \hat{\omega}_m(t))}{b} \tag{4.5}$$

4.2 Sliding Mode Observer

The position being estimated from the back-EMF means a method for calculating and estimating the back-EMF is required. There are various ways of determining the back-EMF based on different observer methods. A common method used in motor control structures are SMO as they have fast performance and ability to deal with model errors, disturbances, and uncertainties [Shtessel et al., 2014]. The overall observer diagram can be seen in fig. 4.3 and consists of the SMO, position calculation, position- and speed PLL.

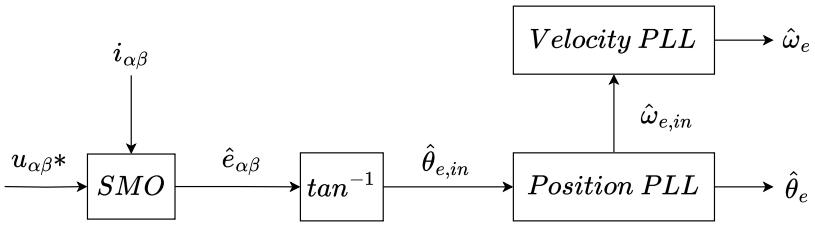

Figure 4.3. *Block diagram of the overall sensorless control with conventional SMO.*

The estimated position might contain noise due to the chattering behavior of the SMO. The noise needs to be filtered and this is done through a PLL, which also extracts the estimated velocity. The extracted velocity also contains noise as it is the output of the position PI controller and it is the derivative of the position. Therefore the velocity is also filtered through a PLL.

The conventional SMO is based on [Qiao et al., 2013], and the approximation of the back-EMF is estimated from the voltage equations stated in eq. (2.9) on page 9. The back-EMF term is then replaced by a switching function given by eq. (4.7), where k is an observer gain and F is a *sign* switching function.

$$\frac{d}{dt}i_{\alpha\beta}(t) = -\frac{R}{L_s}i_{\alpha\beta}(t) + \frac{1}{L_s}u_{\alpha\beta}(t) - \frac{1}{L_s}e_{\alpha\beta}(t) \tag{4.6}$$

$$\hat{e}_{\alpha\beta}(t) = kF(\hat{i}_{\alpha\beta}(t) - i_{\alpha\beta}(t)) \tag{4.7}$$

The sliding surface is defined as in eq. (4.8), where $\hat{i}_s(t)$ is the estimated $\alpha\beta$ currents $\hat{i}_s(t) = [\hat{i}_\alpha(t) \;\; \hat{i}_\beta(t)]^T$ and $i_s(t)$ is the measured current $i_s(t) = [i_\alpha(t) \;\; i_\beta(t)]^T$.

$$S(t, X) = \hat{i}_s(t) - i_s(t) = \bar{i}_s(t) \tag{4.8}$$

The estimated current $\hat{i}_s(t)$ is obtained by inserting the expression of eq. (4.7) into eq. (4.6) resulting in eq. (4.9), which is the conventional SMO. For implementing the conventional SMO in continuous domain the differential operator is replaced by $\frac{d}{dt} = s$ and a block diagram of the conventional SMO can be constructed as in fig. 4.4 on the following page.

$$\frac{d}{dt}\hat{i}_{\alpha\beta}(t) = -\frac{R_s}{L_s}\hat{i}_{\alpha\beta}(t) + \frac{1}{L_s}u_{\alpha\beta}(t) - \frac{1}{L_s}kF(\hat{i}_{\alpha\beta}(t) - i_{\alpha\beta}(t)) \tag{4.9}$$

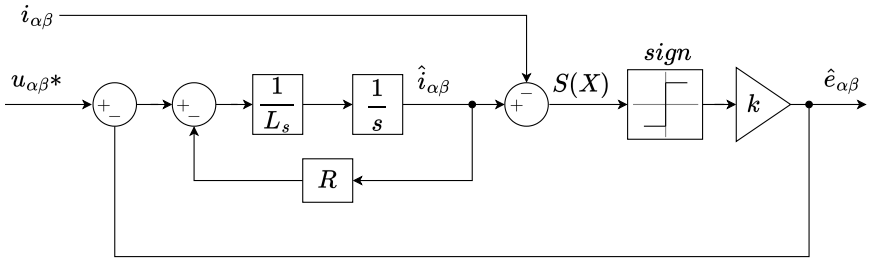

Figure 4.4. *Conventional SMO that estimates the back-EMF.*

The input to the SMO is the voltage references $v^*_{\alpha\beta}(t)$ and the currents $i_{\alpha\beta}(t)$ are the measured *abc* current in the PMSM transformed to the $\alpha\beta$-frame. The output of the observer is the estimated back-EMF $\hat{e}_{\alpha\beta}(t)$. To guarantee stability of the observer the observer gain must satisfy the condition in eq. (4.10) and the stability analysis of the conventional SMO is seen in appendix C on page 66.

$$k > max(|e_\alpha|, |e_\beta|) \tag{4.10}$$

The conventional SMO introduces chattering into the system due to the *sign* function switches discontinuously around zero.

Super Twisting Algorithm

Chattering is a harmful effect because it leads to low control accuracy, high stress on mechanical parts and high power losses in electrical circuits [Utkin, 2011]. The chattering can be reduced in different ways like implementing filters or using higher order SMOs. Filters introduces delay effects and increases the complexity of the system but higher order SMOs can minimize the chattering effects and maintain a simple control structure. A STA is a higher order SMO that have better estimation of the back-EMF and reduce the chattering behavior of the SMO compared to the conventional SMO. The STA is in general form described as in eq. (4.11), where x_i are state variables, $\bar{x}_i$ are error between estimated- and actual state variables, k_i observer gains, ρ_i are perturbation terms and *sign* is the sign function.

$$\begin{aligned} \frac{d}{dt}x_1 &= -k_1|\bar{x}_1|^{1/2}sign(\bar{x}_1) + x_2 + \rho_1(x_1, t) \\ \frac{d}{dt}x_2 &= -k_2 sign(\bar{x}_1) + \rho_2(x_2, t) \end{aligned} \tag{4.11}$$

The STA still uses the *sign* function but it is now continuous as it is either multiplied by $|\bar{x}_1|^{1/2}$ or integrated in x_2. Not having a discontinuous switching function as in eq. (4.7) on the preceding page has the potential of reducing chattering in the SMO, if the observer gains k_i are chosen properly for the system. It has been proven in [Liang et al., 2017a] that if the perturbation terms in eq. (4.12) are globally bounded and the observer gains satisfy the stable condition in eq. (4.13) on the facing page then the system will converge in finite time to the sliding surface. The value δ_1 is any positive number.

$$|\rho_1| \leq \delta_1|x_1|^{1/2},\ \rho_2 = 0 \tag{4.12}$$

$$k_1 > 2\delta_1 \ , \ k_2 > k_1 \frac{5\delta_1 k_1 + 4\delta_1^2}{2(k_1 - 2\delta_1)} \tag{4.13}$$

The perturbation terms are considered as disturbances to the solution of the equation, where the STA is considered the solution. This means that the back-EMF term in eq. (4.6) on page 31 is considered as the solution and thus replaced by the STA, and the terms $\frac{R}{Ls}\hat{i}_{\alpha\beta}(t) + \frac{1}{L_s}u_{\alpha\beta}(t)$ are considered the perturbation terms. This results in a STA-SMO as in as in eq. (4.15), and the perturbation terms ρ_1 and ρ_2 are given by eq. (4.14).

$$\rho_1(\hat{i}_{\alpha\beta}, t) = -\frac{R}{Ls}\hat{i}_{\alpha\beta}(t) + \frac{1}{L_s}u_{\alpha\beta}(t), \quad \rho_2 = 0 \tag{4.14}$$

$$\frac{d}{dt}\hat{i}_{\alpha\beta}(t) = -\frac{R}{L_s}\hat{i}_{\alpha\beta}(t) + \frac{1}{L_s}u_{\alpha\beta}(t) - \frac{1}{L_s}k_1|\bar{i}_s(t)|^{1/2}sign(\bar{i}_s(t)) - \frac{1}{L_s}\int k_2 sign(\bar{i}_s(t))dt \tag{4.15}$$

When the system is stable and converges to the sliding surface the estimation errors are close to the real values and thus the estimated back-EMF can be expressed as in eq. (4.16)

$$\hat{e}_{\alpha\beta}(t) = -k_1|\bar{i}_s(t)|^{1/2}sign(\bar{i}_s(t)) - \int k_2 sign(\bar{i}_s(t))dt \tag{4.16}$$

The two parts of the estimated back-EMF has different properties as the part with k_1 ensure fast dynamic response and the part with integration and k_2 may reduce overall chattering. Usually k_2 is larger than k_1 to minimize steady state chattering. The block diagram of the STA-SMO can be seen in fig. 4.5.

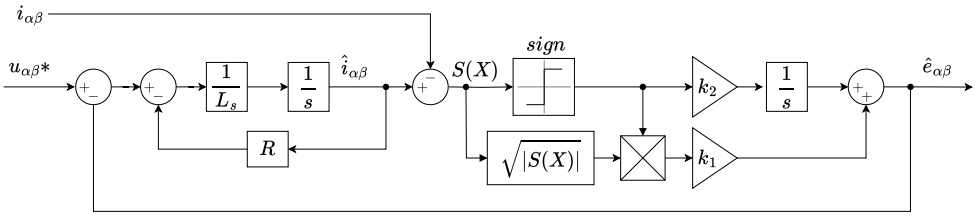

Figure 4.5. *Block diagram of the STA-SMO.*

The proposed STA-SMO uses static observer gains k_1 and k_2 and this means the observer has an optimal working area where the estimated back-EMF is most accurate and has the least chattering. If the PMSM is not operating within the optimal working range the PMSM could potentially become unstable as the position estimation error would be larger as a consequence of an inaccurate or chattering back-EMF estimation. In [Liang et al., 2017b] an adaptive algorithm is proposed for the observer gains k_1 and k_2. This expands the observers ability to estimate accurately the back-EMF and minimize chattering when the PMSM is not operating around specific velocities related to k_1 and k_2. The proposed adaptive observer gains are multiplying a factor σ_1 and σ_2 with the estimated electrical velocity $\hat{\omega}_e(t)$ as in eq. (4.17).

$$k_1 = \sigma_1\hat{\omega}_e(t), \quad k_2 = \sigma_2\hat{\omega}_e(t)^2 \tag{4.17}$$

This means that the values of σ_1 and σ_2 are used as a working point around some chosen operating velocity. The coefficients σ_1 and σ_2 can then be found by choosing an operating velocity ω_0 and corresponding observer gains k_{10} and k_{20} that fulfills the stability criteria in eq. (4.13) on the previous page and minimizes chattering at this velocity.

$$\sigma_1 = \frac{k_{10}}{\omega_0}, \quad \sigma_2 = \frac{k_{20}}{\omega_0^2} \tag{4.18}$$

In fig. 4.6 is a block diagram of the STA-SMO with adaptive coefficients. In fig. 4.7 is a simulation comparison between the estimated back-EMF α component $\hat{e}_\alpha(t)$ at different steady state velocities for static and adaptive observer gains for. The simulation is made to see how the observer performs close to 1200 RPM and further away. In theory the performance between the static and adaptive coefficients should be similar at 1200 RPM and then have some deviations at velocities away from 1200 RPM.

The observer gains are $k_1 = 12$ and $k_2 = 50000$ and they are found iterative at the operating velocity of $\omega_0 = 1200$ RPM. The adaptive coefficients are found by using $k_{10} = k_1$ and $k_{20} = k_2$ and insert into eq. (4.18) with $\omega_0 = 1200$ RPM. The measured value of the back-EMF in the simulations are found by $e_\alpha(t) = -\lambda_{mpm}\omega_e(t)sin(\theta_e(t))$ and is calculated by using the measured position and velocity by the encoder.

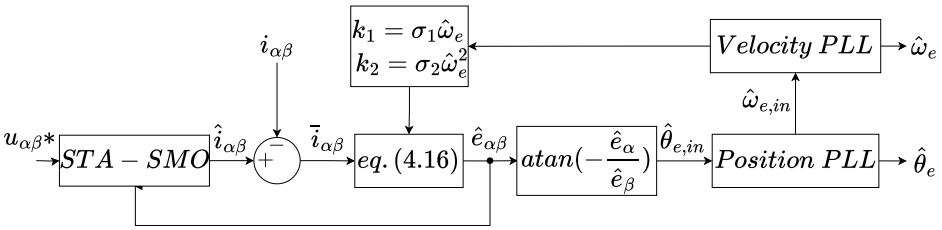

Figure 4.6. *Block diagram of the STA-SMO with adaptive observer gains.*

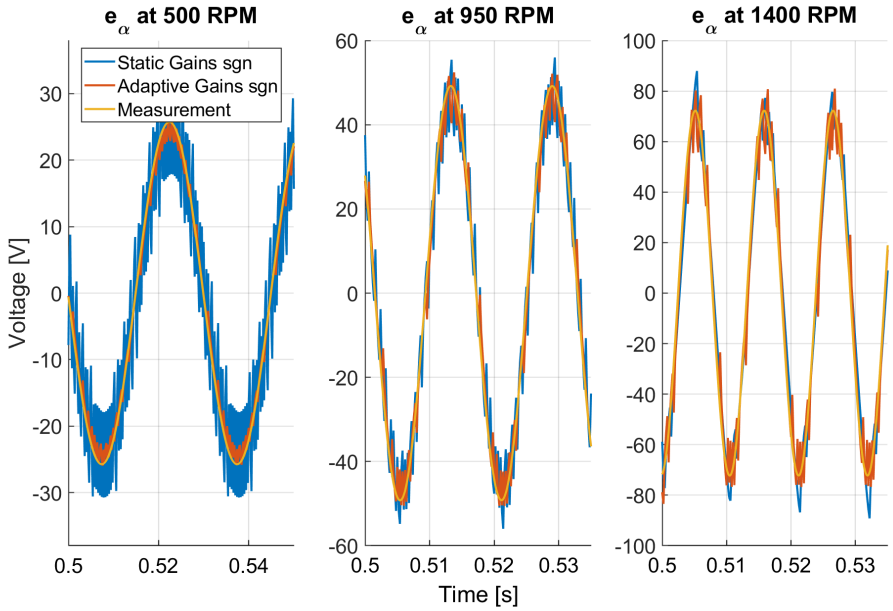

Figure 4.7. *Chattering using a sign function with static- and adaptive gains k_1 and k_2.*

It can be seen in fig. 4.7 that having adaptive observer gains improves the performance at lower velocities compared to the observer with static gains. The performances at 1400 RPM are similar, which aligns with the operating velocity being $\omega_0 = 1200$ RPM. At

950 RPM the adaptive gains has less chattering compared to the observer with static gains. At 500 RPM the adaptive gains are estimating the back-EMF with far less ripples compared to the static gains.

The chattering is reduced with the adaptive observer gains, but can be further improved by changing the switching function from a *sign* function to a *sigmoid* function. The function is seen in eq. (4.19)

$$F(x) = \frac{2}{1 + e^{-ax}} - 1 \tag{4.19}$$

The *sigmoid* function is differentiable and continuous around zero, and the slope can be adjusted by the parameter a. Implementing the *sigmoid* switching function a comparison is again made for the estimated back-EMF $\hat{e}_\alpha(t)$ comparing the effect of the switching function still using adaptive STA-SMO coefficients. The adjustable parameter of the *sigmoid* switching function is $a = 0.8$.

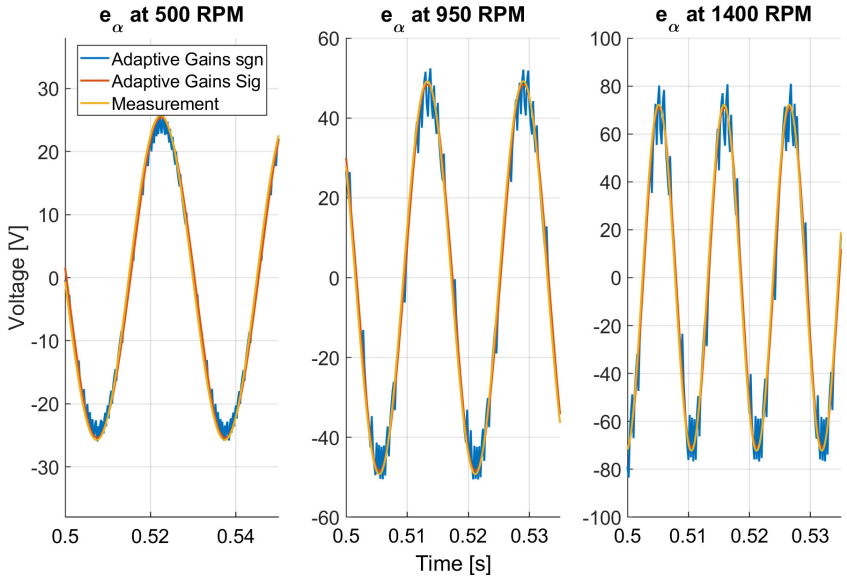

Figure 4.8. *Chattering comparison between adaptive sigmoid- and sign switching function.*

The chattering behavior has been improved at all velocities by changing the switching function from a *sign*- to a *sigmoid* function. It is clear that using a *sigmoid* switching function in the adaptive STA-SMO gives the best estimation of the back-EMF $\hat{e}_{\alpha\beta}(t)$. This method is used for the senseless drive and the estimated rotor position $\hat{\theta}_e(t)$ can then be calculated based on the estimated back-EMF and filtered using a PLL.

4.3 Phase Locked Loop

The position and velocity estimation is based on PLL. A PLL is a filter structure that has similar characteristics as a LPF without phase-shift. The PLL locks onto the input frequency, while still removing undesired high frequency components above the cutoff frequency of the PLL. The structure of the PLL can be seen in fig. 4.9 on the next page. [Wang et al., 2017]

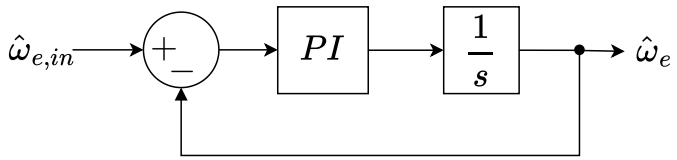

Figure 4.9. *PLL block diagram with velocity $\hat{\omega}_e$ as input.*

The PLL's input signal is sent through a PI controller, integrated and fed back to the input. This way the output's phase is synchronized with the reference signal. Tuning the PI controller effectively changes the cutoff frequency of the PLL. Designing the PLL is done by following the method in [Wang et al., 2017], where it is shown that the cutoff frequency of the PLL has a close to linear relationship between the PI controller gains $K_{P,PLL}$ and $K_{I,PLL}$. The closed loop transfer function of the PLL can be seen in eq. (4.20).

$$H_{PLL}(s) = \frac{K_{P,PLL} \cdot s + K_{I,PLL}}{s^2 + K_{P,PLL} \cdot s + K_{I,PLL}} \tag{4.20}$$

The closed loop transfer function is then solved for the cutoff frequency defined as $-3dB = \frac{1}{\sqrt{2}}$. This is done to find a relationship between the PLL gains $K_{P,PLL}$ and $K_{I,PLL}$.

$$|H_{PLL}(j \cdot \omega c_{PLL})| = \left| \frac{K_{P,PLL} \cdot j \cdot \omega c_{PLL} K_{I,PLL}}{(j \cdot \omega c_{PLL})^2 + K_{P,PLL} \cdot j \cdot \omega c_{PLL} + K_{I,PLL}} \right| = \frac{1}{\sqrt{2}} \tag{4.21}$$

Solving eq. (4.21) gives the expression for the cut-off frequency in eq. (4.22), which can be further simplified if it is assumed a linear relation exists between $K_{P,PLL}$ and $K_{I,PLL}$. The linear relation is determined by the variable a_{PLL} and the controller gains can then be found in eq. (4.23) by choosing a desired cutoff frequency ωc_{PLL} and a value of a_{PLL}.

$$\omega c_{PLL} = \sqrt{\frac{K_{P,PLL}^2 + 2 \cdot K_{I,PLL} + \sqrt{(K_{P,PLL}^2 + 2 \cdot K_{I,PLL})^2 + 4 \cdot K_{I,PLL}^2}}{2}} \tag{4.22}$$

$$K_{I,PLL} = K_{P,PLL} \cdot a_{PLL} \qquad \omega c_{PLL} \approx K_{P,PLL} + a_{PLL} \tag{4.23}$$

4.4 Position Estimation

The estimated back-EMF from the STA-SMO is used to estimate the rotor position. This is done through an *atan* function and filtered through the PLL as illustrated in fig. 4.10 on the facing page. The position PLL includes a sinuous function and a reset block that ensures the position ranges from 0 to 2π. Furthermore the output of the PI controller is the estimated speed $\hat{\omega}_e(t)$, which is sent through a velocity PLL.

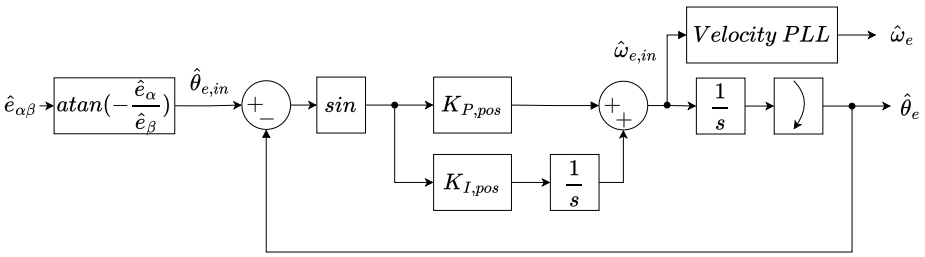

Figure 4.10. *Block diagram of the position PLL.*

Tuning the PI coefficients is done using the linear method described in eq. (4.23) on the preceding page. When choosing a cutoff frequency of the PLL there is a trade-off between faster dynamics in the transient response and steady state ripples. The tuning process is done by iterative changing the cutoff frequency and three different cutoff frequencies are illustrated in fig. 4.11. The test is made with the encoder as feedback and a load step change of 5 Nm. The STA-SMO and position PLL is computed parallel to the system to have same test environment for the PLL. The position estimation error is used as performance parameter comparing the different cut-off frequencies. The position estimation error is the error between the encoder position and output of the PLL structure above and given by $\hat{\theta}_{error}(t) = \theta_e(t) - \hat{\theta}_e(t)$.

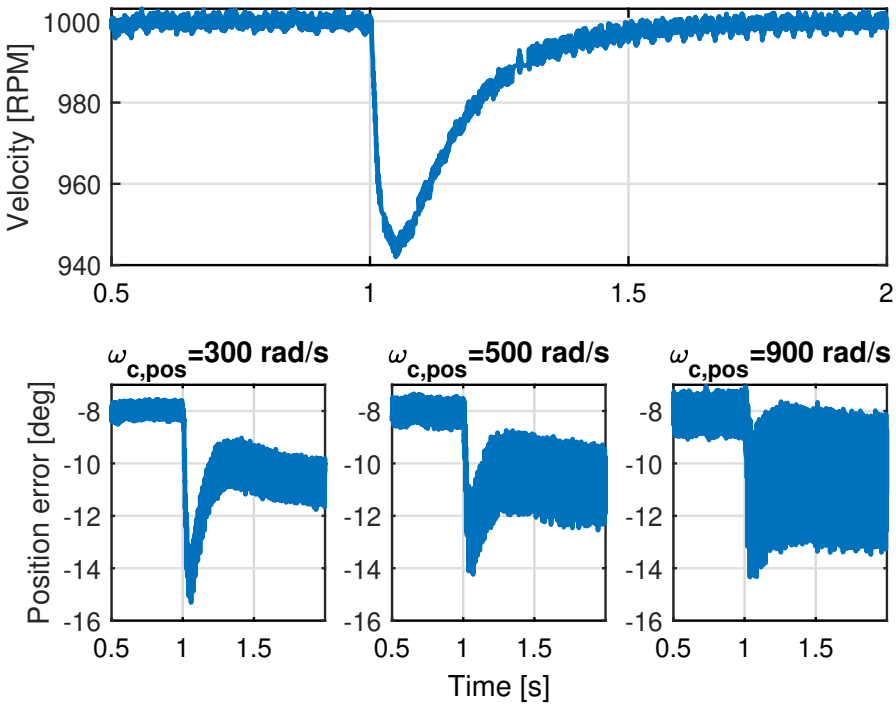

Figure 4.11. *Position PLL performances at different cutoff frequencies, with a 5 Nm load change.*

The results in fig. 4.11 shows that the ripples are lower in amplitude at a the low cutoff frequency $\omega_{c,pos} = 300\frac{rad}{s}$ compared to the higher cutoff frequencies. The transient response is faster at the higher frequencies of 500 and $900\frac{rad}{s}$ compared to the lower, which can be seen by the position error has the largest drop to approximately $-15°$ compared to $-14°$ at 500 and 900 $\frac{rad}{s}$. The position estimation error graph also indicates two things. First, there is a DC-offset in the position estimation error in fig. 4.11 and this indicates that there might be some calculation delay between the measured value of the encoder and the rotor position estimation. Second, the position estimation error

changes from $-8°$ to $-11°$ at steady state after the load change. This could indicate by looking at fig. 4.1 on page 29 that the inductance parameter L_s is inaccurate. The load change results in a higher current, and thus the reactance part, the orange dashed line with $j\omega L_s i_{\alpha\beta}$, might not align with the q-axis, if L_s is inaccurate. This could lead to the position estimation error changes at steady state after a load input.

Deciding which cut-off frequency should be used must be put into the context of the thesis. The goal is to use ADRC in a sensorless application and there is a trade-off between performance and steady state ripples when designing the PLL. This means the estimated position is used as the rotor position for reference frame transformation and to extract the velocity of the PMSM. The ADRC uses the load compensation by a feedforward signal, meaning a chattering velocity estimation based on the position is feed directly into the input of the PMSM. Therefore there is an argument for choosing the cutoff with least steady state ripples, but having a slow response resulting in larger errors that needs to be compensated can also cause delays due to longer convergence time, which might result in transient oscillations. Therefore it is reasonable to choose the cut-off frequency at $\omega_{c,pos} = 500\frac{rad}{s}$ as it has faster transient response than the cut-off at $300\frac{rad}{s}$ and better noise attenuation compared to $900\frac{rad}{s}$. Therefore the position PLL with $\omega_{c,pos} = 500\frac{rad}{s}$ is used as the position filter for the sensorless drive and the PLL gains are $K_{P,pos} = 495$ and $K_{I,pos} = 2475$.

4.5 Velocity Estimation

The output of the position PLL PI in fig. 4.10 on the preceding page is the estimated velocity that is used for sensorless control. The estimated velocity needs to be further filtered through another PLL to further reduce noise of the estimated velocity. The cutoff frequency has been chosen to be $\omega_{c,vel} = 100\frac{rad}{s}$ with gains of $K_{P,vel} = 95$, $K_{I,vel} = 475$ and has been determined in a similar way as the cutoff frequency of the position estimation. Increasing the $\omega_{c,vel}$ above 100 $\frac{rad}{s}$ would result in a faster response but with more ripples, which is harmful to the mechanical components. The opposite is the case if $\omega_{c,vel}$ is lowered below $100\frac{rad}{s}$ that the transient response becomes slower and might introduce transient oscillations, but could improve the steady state ripples. In fig. 4.12 on the next page a load step change response of the actual system with encoder feedback can be seen.

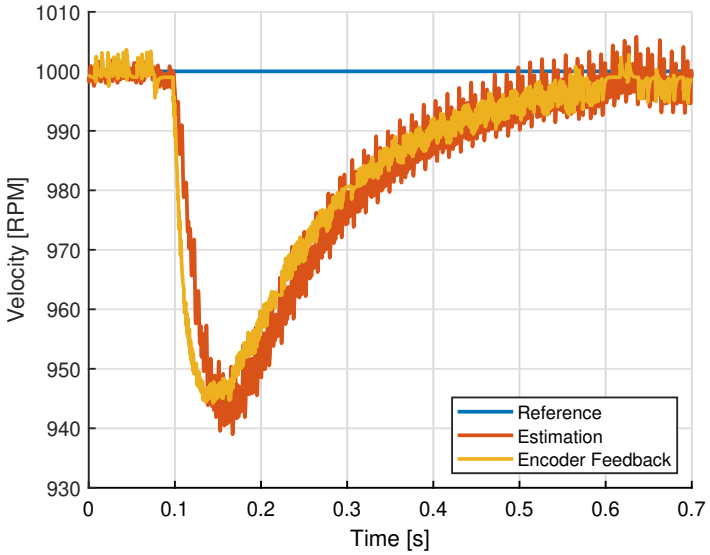

Figure 4.12. *Velocity load change from 0 to 5 Nm with encoder feedback.*

The velocity estimation of the load change in fig. 4.12 illustrates that the estimated velocity is delayed compared to the measured velocity. The delay could be optimized by increasing the cut-off frequencies of the position- and velocity estimation, but this would also introduce more chattering into the system. The steady state ripples of the estimated velocity is comparable to the measured velocity at no-load, but after the load change occurs the estimated velocity has more ripples compared to the measured velocity. The Ripples are $\pm 0.5\%$ of the reference velocity and could be further minimized by lowering the cutoff frequency with the cost of slower dynamic response. Therefore the cut-off frequency of $\omega_{c,vel} = 100\frac{rad}{s}$ has been found to be a compromise between fast dynamics and steady state ripples and is used for the sensorless control.

This concludes the design of the sensorless control, which is based on a STA-SMO with adaptive observer gains and PLLs for position and velocity extraction. The sensorless control is tested with the velocity PI controller to test and validate the performance in the experimental setup and compare it with simulations.

4.6 Sensorless Control Validation

The sensorless control is tested in lab and compared to the performance with encoder feedback. Simulation results will also be illustrated in the graphs to validate the simulation model has a similar performance as in the lab.

Normally when a motor is running with a sensorless application it needs a startup method as the sensorless control is inaccurate at low speed. One method could be, as in [Wang et al., 2012], to use I/F control to ramp up the speed with a fixed i_q current. When the velocity is above the low speed range it is kept at a certain reference velocity. Then the i_q current reference is slowly decreased, while the velocity reference is maintained until the estimated rotor position and the rotor position from the I/F startup are equal to each other. However the experimental setup has an encoder installed, which enables easier startup by using encoder feedback for startup. Then switching over to the snesorless drive ones the PMSM has been accelerated above the low speed region ($\geq$ 10% rated speed), which for this PMSM is at 450 RPM as the rated speed is 4500 RPM.

The full drive cycle is then tested in chapter 5 on page 43, but to validate the performance of the sensorless drive a load- and no-load test are performed with the PI controller. The first test is a no-load test where the velocity reference is ramped from 500 RPM to 1200 RPM. The second test is a load change of 10 Nm at 1200 RPM. The no-load test result can be seen seen in fig. 4.13, where FB and Sim in the legend is used as abbreviations for feedback and simulation respectively.

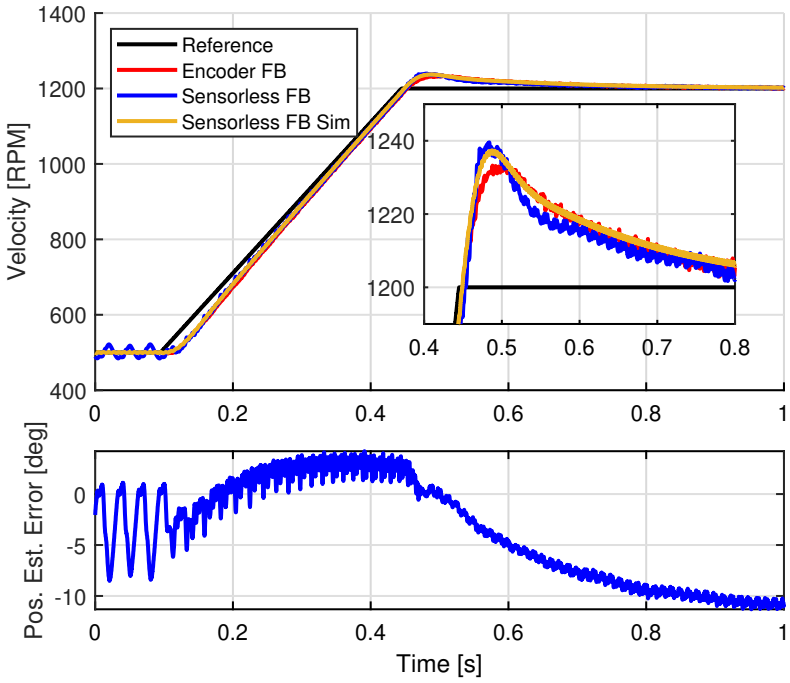

Figure 4.13. *Velocity change test with velocity PI controller using sensorless- or encoder feedback. Position estimation error is with sensorless feedback.*

The velocity change test illustrates overall the performance between the sensorless- and encoder velocity feedback are comparable. Some deviations occur in the steady state performance at low speed and the transient response when the ramp meets its reference. At low speed the sensorless control has large oscillations. The simulations of the estimated back-EMF in fig. 4.8 on page 35 indicates that the back-EMF is well estimated by the STA-SMO. This leads to a possible reason for the steady state ripples occurs from the velocity PLL parameters being static, which might have too high a cut-off frequency for this velocity, which leads to steady state oscillations. The PMSM is still stable at 500 RPM and thus it is still considered to be acceptable as the remaining of the drivecycle in fig. 3.7 on page 25 is above 500 RPM and no oscillation occur at 1200 RPM.
A closer look at the ramp- and transient response shows that the sensorless control has a larger overshoot than the encoder feedback and the ramp slopes are comparable. The ramp slopes of the encoder- and sensorless feedback being similar, means the PI output of the velocity controls are similar, and thus it is only when the ramp reference change the responses are different, which again could be caused by the cutoff frequency of the PLL. The LPF for the encoder has a cutoff frequency of 100 Hz and the velocity PLL is at $100\frac{rad}{s}$ meaning 15.9 Hz. Therefore it is likely the slower transient response arises from a lower cutoff frequency of the filter compared to the encoder. The larger overshoot for the sensorless control could similarly arise from having a lower PLL cutoff frequency compared to the LPF for the encoder. This causes an overshoot and larger current compensation afterwards, which results in slight oscillations in the transient response.

The settling times are similar between the sensorless- and encoder feedback. A load change test of 10 Nm is also made and seen in fig. 4.14.

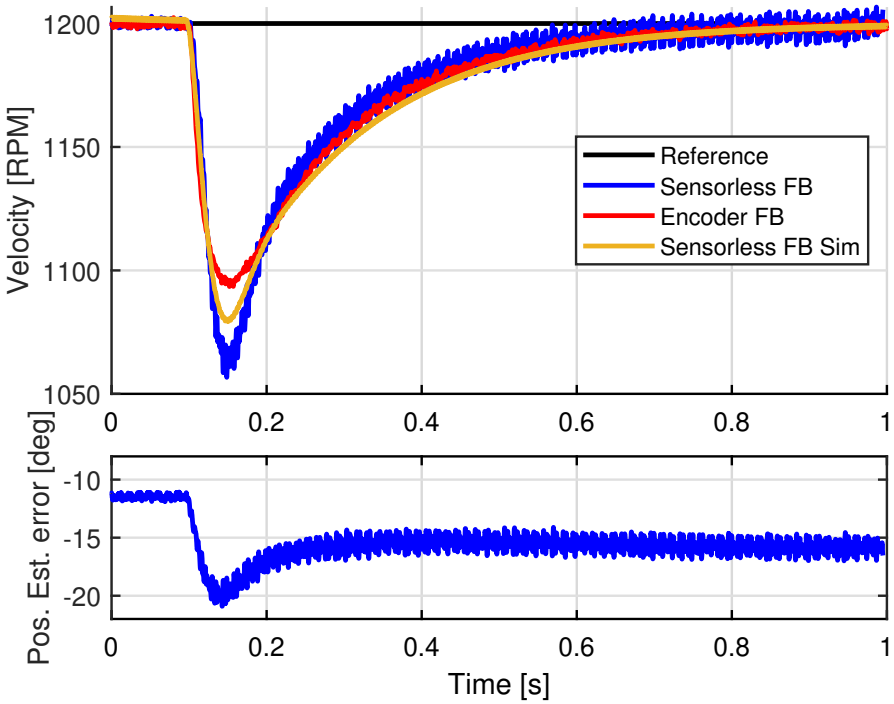

Figure 4.14. *Load change test with PI controller and sensorless- or encoder feedback. Position estimation error is with sensorless feedback.*

The results of the 10 Nm load test shows that the sensorless control reacts slower to the load change than the encoder feedback. This could again be caused by the lower cutoff frequency of the velocity filter, which results in a greater velocity drop before the velocity error is compensated. The transient phase is without oscillations and the settling times are similar between the encoder- and sensorless control. The sensorless control has increased ripples at steady state after the load change, which likely is caused by the increased position estimation error the load change causes as it can be seen in the lower graph of fig. 4.14. The steady state oscillations are ± 6 RPM, which is 0.5% of the reference speed and is within an acceptable range. Looking at the position estimation error it can be seen the DC-offset at $t = 0s$ is greater than in fig. 4.11 on page 37 at $t = 0s$. This could again indicate that there is a calculation delay, which in fig. 4.14 results in an position estimation error of $\approx -11^\circ$ compared to $\approx -8^\circ$ in fig. 4.11 on page 37. The calculation delay remain constant, but the velocity increases and thus a larger position estimation error is seen at 1200 RPM compared to 1000 RPM. Potential improvements in the position estimation error is discussed in chapter 6 on page 54. Also the position estimation error is increased after the load change at steady state, which is also the case for fig. 4.11 on page 37.
The load change in the simulation model has a faster response than the sensorless experimental setup, and this could be caused by parameter uncertainties or unmodelled dynamics of the IM machine or inverter. The simulation results are thus still in the vicinity of the real experiment and is thus validated through the load- and no-load tests.

The performance of the sensorless control in the experimental setup and simulations show, that the STA-SMO and PLLs for extracting rotor position and velocity can run the PMSM. The different gains used for the PLLs and the STA-SMO is listed in table 4.1. The

performance deviations are found to be limited by the cut-off frequency of the velocity PLL as increasing it higher than $100\frac{rad}{s}$ would result in more steady state ripples, which in a loaded situation in fig. 4.14 on the previous page resulted in ripples of $\pm 0.5\%$ of the reference speed. Therefore the sensorless control is further analysed in combination with the ADRC before implementing it into the experimental setup. This is done by making a disturbance- and noise analysis of the system and is described in the following chapter.

	$STA-SMO$				$Position\ PLL$			$Velocity\ PLL$		
Parameter	a	k_1	k_2	ω_0	$\omega_{c,pos}$	$K_{P,pos}$	$K_{I,pos}$	$\omega_{c,vel}$	$K_{P,vel}$	$K_{I,vel}$
Value	0.8	12	50000	1200	500	495	2475	100	95	475

Table 4.1. *Parameters used for the sensorless drive.*

ADRC Sensorless Control 5

In this chapter the ADRC described in chapter 3 on page 15 and the sensorless control described in chapter 4 on page 29 are combined, analysed, simulated and tested in the lab. An analysis is made of how the velocity estimation's PLL influences the dynamics and performances of the ADRC controllers as this seems to be the limiting factor in the sensorless PI validation in section 4.6 on page 39. The drivecycle test in fig. 3.7 on page 25 is also performed for the ADRC controllers with sensorless feedback and compared to the encoder feedback.

5.1 PLL Influence on Performance

Combining the ADRC with the sensorless control is done by changing the signals sent through the switch in fig. 5.1 such that the estimated velocity $\hat{\omega}_m(t)$ is used as feedback and estimated rotor position $\hat{\theta}_e(t)$ is used for reference frame transformations.

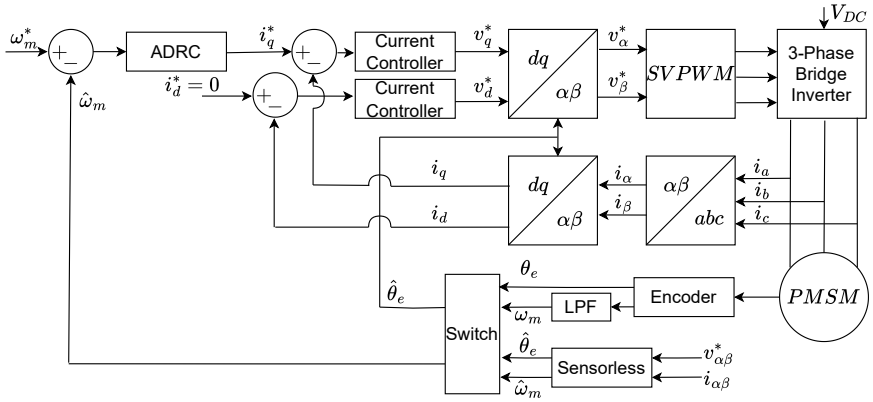

Figure 5.1. *ADRC with $\hat{\omega}_m$ and $\hat{\theta}_e()$ passed through the switch for sensorless feedback.*

To analyse how the sensorless application influences the disturbance rejection and noise attenuation of the ADRCs some simplifications are made to derive new expressions for their closed-loop transfer functions. The inner current loops are assumed to be without influence on the outer loop performance and is considered unity gain. The input gain b is assumed to be without parameter deviations compared to the actual system. It is assumed the rotor position estimation $\hat{\theta}_e(t)$ is ideal, meaning $\hat{i}_q(t) = i_q(t)$, and the position PLL cut-off frequency has no influence on the controller performance. This leaves the velocity estimation as the only potential influence on the system. The velocity estimation is based on the PLL described in chapter 4 on page 29, and implementing a PLL into the block diagram, of fig. B.1 on page 62, which is based on $d(t)$ as input and leaving $\omega_m^*(t)$ and $\delta(t)$ equal zero, results in a simplified block diagram of the ADRC with sensorless control in fig. 5.2 on the next page.

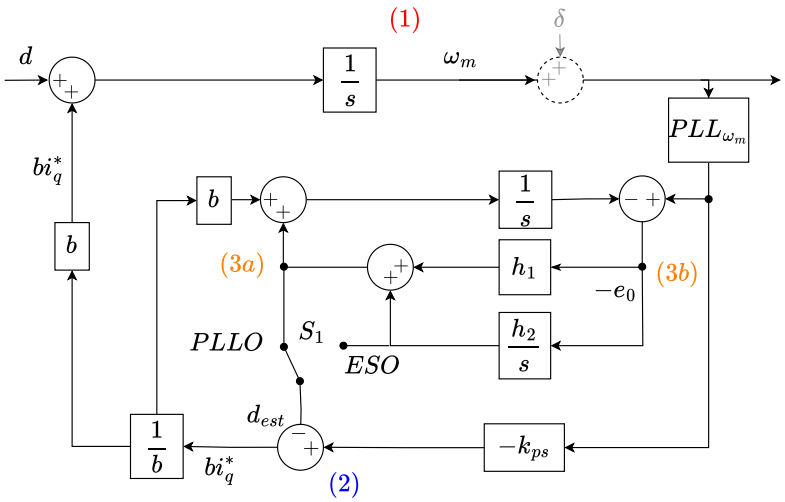

Figure 5.2. *ADRC block diagram with d as input and a PLL for velocity estimation.*

The closed loop transfer functions of the $PLLO$ is changed due to the implementation of the PLL. The derivation can similarly be derived, as in appendix B on page 61, by stating the equations for part (1), (2) and (3a) in fig. 5.2 as below.

$$(1) \quad \frac{1}{s}(d + bi_q^*) = \omega_m \tag{5.1}$$

$$(2) \quad -k_{ps}\omega_m PLL_{\omega_m} - d_{est} = bi_q^* \tag{5.2}$$

$$(3a) \quad [\omega_m PLL_{\omega_m} - \frac{1}{s}(bi_q^* + d_{est})](h_1 + \frac{h_2}{s}) = d_{est} \tag{5.3}$$

The derivation is the same as in appendix B on page 61 and this results in a disturbance closed-loop expression as in eq. (5.4).

$$\frac{\omega_m(s)}{d(s)} = \frac{s^2}{s^3 + PLL_{\omega_m}((h_1 + k_{ps})s^2 + (k_{ps}h_1 + h_2)s + h_2 k_{ps})} \tag{5.4}$$

The characteristic equation of the transfer function in eq. (5.4) is not easily compared to the disturbance transfer function in eq. (3.24) on page 20 without PLL. However it is possible to modify the characteristic equation by adding $(1 - PLL_{\omega_m})s^3$ in the denominator as in eq. (5.5).

$$\frac{\omega_m(s)}{d(s)} = \frac{s^2}{PLL_{\omega_m}(s^2 + h_1 s + h_2)(K_{ps} + s) + (1 - PLL_{\omega_m})s^3} \tag{5.5}$$

This gives a more intuitive comparison between the disturbance transfer functions with- and without PLL and the added term equals zero if the PLL can be considered a unity gain. This of course depends on the cut-off frequency of the PLL.
Similarly can the closed-loop disturbance rejection response be derived for the ESO by connecting the switch S_1 to ESO and restating equation (1), (2) and (3b) from fig. 5.2.

$$(1) \quad \frac{1}{s}(d + bi_q^*) = \omega_m \tag{5.6}$$

$$(2) \quad -k_{ps}\omega_m PLL_{\omega_m} - (-e_0)(h_1 + \frac{h_2}{s}) = bi_q^* \tag{5.7}$$

$$(3b) \quad \omega_m PLL_{\omega_m} - \frac{1}{s}(bi_q^* + (-e_0)(h_1 + \frac{h_2}{s})) = -e_0 \tag{5.8}$$

Following the approach in appendix B on page 64 for the ESO results in the disturbance closed loop transfer function with PLL and is written in eq. (5.9). The ESO characteristic equation is also added with the terms $(1-PLL_{\omega_m})s^3$ and $(1-PLL_{\omega_m})h_1s^2$ to have better comparison of the characteristic equations.

$$\frac{\omega_m(s)}{d(s)} = \frac{s(s+h_1)}{PLL_{\omega_m}(s^2+h_1s+h_2)(K_{ps}+s)+(1-PLL_{\omega_m})s^3+(1-PLL_{\omega_m})h_1s^2} \tag{5.9}$$

The PI controller is also added a PLL into its loop to estimate the sensorless PI disturbance response and in eq. (5.10) are all the response listed.

$$\Phi_d(s) = \begin{cases} \dfrac{s}{s^2+(k_{ps}s+k_{is})PLL_{\omega_m}} & PI \\ \dfrac{s(s+h_1)}{PLL_{\omega_m}(s^2+h_1s+h_2)(K_{ps}+s)+(1-PLL_{\omega_m})s^3+(1-PLL_{\omega_m})h_1s^2} & ESO \\ \dfrac{s^2}{PLL_{\omega_m}(s^2+h_1s+h_2)(K_{ps}+s)+(1-PLL_{\omega_m})s^3} & PLLO \end{cases} \tag{5.10}$$

Comparing the closed-loop transfer functions with velocity PLL in eq. (5.10) to the disturbance transfer functions with encoder feedback in eq. (3.29) on page 21, it is clear, that if the PLL's cut-off frequency is fast enough to be without influence the transfer functions in eq. (5.10) simplifies to the transfer functions in eq. (3.29) on page 21. However if this is not the case there is a risk of the transient- and steady state performance change and degrade. Looking at the denominator of the closed-loop transfer functions in eq. (5.10) it can be seen, that the $PLLO$'s denominator terms, except s^3, are influenced by the PLL. The ESO has two terms without PLL influence, which is s^3 and h_1s^2. This means the proportional term h_1 within the observer PI is not influenced by the velocity PLL for the ESO. The h_1 term being responsible for fast transient dynamics and steady state ripples if it is to aggressive means, there might be a smaller risk of the PLL influencing the transient dynamics of the ESO compared to the $PLLO$. The PLL is also changing the dynamics of the PI poles, and again the PLL influence depends on the cutoff frequency of the PLL. The disturbance closed-loop transfer functions are plotted using the same parameters for the ADRC controllers as in table 3.1 on page 21 and the coefficients for the PLL is as in table 4.1 on page 42. The dashed lines are the closed-loop transfer functions in eq. (3.29) on page 21 for comparison.

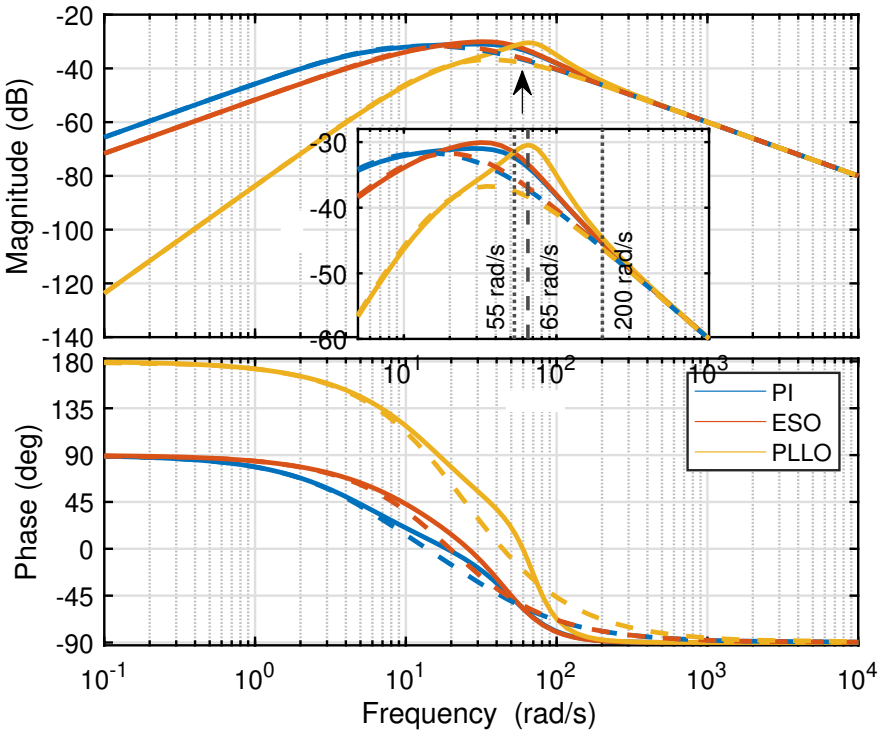

Figure 5.3. *Bode plots for the closed-loop sensorless disturbance rejection.*

The bode plot illustrates that by only taking into consideration that there is a PLL with a cutoff frequency of $\omega_{c,vel} = 100\frac{rad}{s}$ the dynamics change. Most significant is it for the $PLLO$ where there is a peak value $\approx 65\frac{rad}{s}$, illustrated by a dashed line in the zoom view, which is not seen in the response without the velocity PLL. This indicates that the $PLLO$ might oscillate as the controller rejects a load due to the frequencies around $65\frac{rad}{s}$ are amplified compared to the dashed $PLLO$ encoder feedback. The PI and ESO have more comparable bode plots with the transfer functions in eq. (3.29) on page 21 and it is not certain, by only analysing the influence of the velocity PLL, if the sensorless drive changes the disturbance rejection dynamics of the ESO and PI. The $PLLO$ still rejects disturbances better below $55\frac{rad}{s}$, but if the disturbance frequency is in the range of 55 - $200\frac{rad}{s}$, illustrated by the dotted lines in the zoomed view, the ESO and PI are now better at rejecting these disturbances whereas without velocity PLL the $PLLO$'s disturbance rejection is better in this frequency range as well.

Plotting the unity step input responses of the disturbance rejection closed-loop transfer functions results in the responses in fig. 5.4 on the facing page.

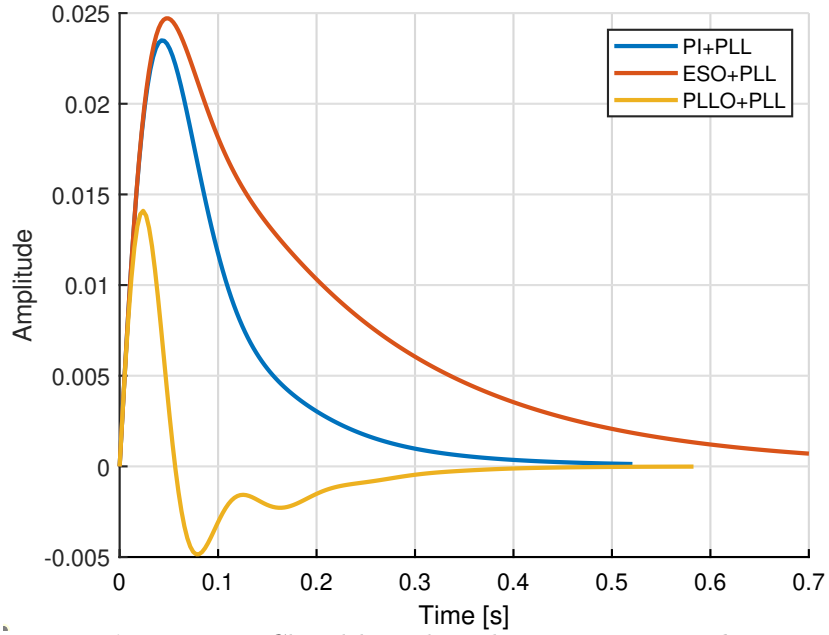

Figure 5.4. *Closed-loop disturbance response with PLL.*

The unity step input responses indicate that the sensorless $PLLO$ will have oscillations in the transient performance compared to the tests with encoder feedback in fig. 3.5 on page 23. The velocity drops are also expected to be larger when the PLL is implemented, but the settling time is expected to be the same as with encoder feedback. The ESO and PI controllers are expected to also have a larger velocity drop compared to the encoder feedback in fig. 3.5 on page 23. The transient responses of the ESO and PI are however expected to not overshoot the reference, as with encoder feedback, and not contain transient oscillations, if the velocity PLL is the only influence from the sensorless application.

However as the position PLL designed in section 4.4 on page 36 has a cut-off frequency of $\omega_{c,pos} = 500\frac{rad}{s}$, which is lower than the encoder LPF at 100 Hz, it will likely degrade the performance of the disturbance rejection even more than seen in fig. 5.4. Furthermore it has been in seen in fig. 4.14 on page 41, that the position estimation error might become -16° when the load applied from the IM is 10 Nm at 1200 RPM. When this is the case and inserting the position estimation error into the d- and q-axis equations in eq. (4.2) on page 30 and eq. (4.3) on page 30 would result in some of the current being placed on the d-axis. As FOC aims to maintain $i_d = 0$ more chattering and current might be used compared to if the position estimation error was closer to zero. Furthermore if the ADRC input gain b has parameter deviations compared to the experimental setup the performance might also deviate further compared to the performance in fig. 5.4.

The performance of fig. 5.4 is based on the assumptions that the input gain b and position estimation is ideal, $\hat{i}_q(t) = i_q(t)$ and the inner current loop can be considered as a unity gain. These assumptions are discussed above and thus the step responses are considered the optimal case for a velocity PLL with $\omega_{c,vel} = 100\frac{rad}{s}$. That being said it is still expected the velocity PLL has the largest influence on the overall performance deviations that might occur between the encoder- and sensorless feedback.

Noise Transfer Functions

The noise transfer functions are also augmented by the implementation of the PLL, and they are derived by letting $d = 0$ in fig. 5.2 on page 44 and letting δ being the input. Starting by the noise closed-loop transfer function for the $PLLO$ the starting equations are given by eq. (5.11), (5.12) and (5.13), where the PLL is added to equation (2) and (3a).

$$(1) \quad \frac{1}{s} b i_q^* = \omega_m \tag{5.11}$$

$$(2) \quad -k_{ps}(\omega_m + \delta) PLL_{\omega_m} - d_{est} = b i_q^* \tag{5.12}$$

$$(3a) \quad [(\omega_m + \delta) PLL_{\omega_m} - \frac{1}{s}(b i_q^* + d_{est})](h_1 + \frac{h_2}{s}) = d_{est} \tag{5.13}$$

Using these starting equations results in a noise closed-loop transfer function for the $PLLO$ as in eq. (5.14).

$$\frac{\omega_m(s)}{\delta(s)} = -\frac{PLL_{\omega_m}((h_1 + k_{ps})s^2 + (h_1 k_{ps} + h_2)s + h_2 k_{ps})}{s^3 + PLL_{\omega_m}((h_1 + k_{ps})s^2 + (h_1 k_{ps} + h_2)s + h_2 k_{ps})} \tag{5.14}$$

The denominator is the same as for the disturbance transfer function, and thus it can be simplified by adding the term $(1 - PLL_{\omega_m})s^3$. Furthermore looking at the term s^3 in the denominator it is the only term missing in the nominator. This means the transfer function can be simplified by having a positive term with s^3 and minus by 1 as in eq. (5.15)

$$\frac{\omega_m(s)}{\delta(s)} = \frac{s^3}{PLL_{\omega_m}(s^2 + h_1 s + h_2)(K_{ps} + s) + (1 - PLL_{\omega_m})s^3} - 1 \tag{5.15}$$

Similarly the ESO noise closed-loop response can be derived based on the derivation in appendix B on page 64, and the starting equations for the ESO is given by eq. (5.16), (5.17) and (5.18).

$$(1) \quad \frac{1}{s} b i_q^* = \omega_m \tag{5.16}$$

$$(2) \quad -k_{ps}(\omega_m + \delta) PLL_{\omega_m} - (-e_0)(h_1 + \frac{h_2}{s}) = b i_q^* \tag{5.17}$$

$$(3b) \quad (\omega_m + \delta) PLL_{\omega_m} - \frac{1}{s}(b i_q^* + (-e_0)(h_1 + \frac{h_2}{s})) = -e_0 \tag{5.18}$$

From these equations the transfer function of the ESO noise attenuation can be derived and the simplified expression is given in eq. (5.19) on the facing page.

$$\frac{\omega_m(s)}{\delta(s)} = -\frac{s^2(h_1 s + 1)}{PLL_{\omega_m}(s^2 + h_1 s + h_2)(K_{ps} + s) + (1 - PLL_{\omega_m})s^3 + (1 - PLL_{\omega_m})h_1 s^2} - 1$$

(5.19)

The closed-loop noise transfer function are listed in eq. (5.20) and their bode plots are illustrated below in fig. 5.5.

$$\Phi_\delta(s) = \begin{cases} -\dfrac{K_{is} + K_{ps}s}{s^2 + (k_{ps}s + k_{is})PLL_{\omega_m}} & PI \\ \dfrac{s^2(h_1 s + 1)}{PLL_{\omega_m}(s^2 + h_1 s + h_2)(K_{ps} + s) + (1 - PLL_{\omega_m})s^3 + (1 - PLL_{\omega_m})h_1 s^2} - 1 & ESO \\ \dfrac{s^3}{PLL_{\omega_m}(s^2 + h_1 s + h_2)(K_{ps} + s) + (1 - PLL_{\omega_m})s^3} - 1 & PLLO \end{cases} \tag{5.20}$$

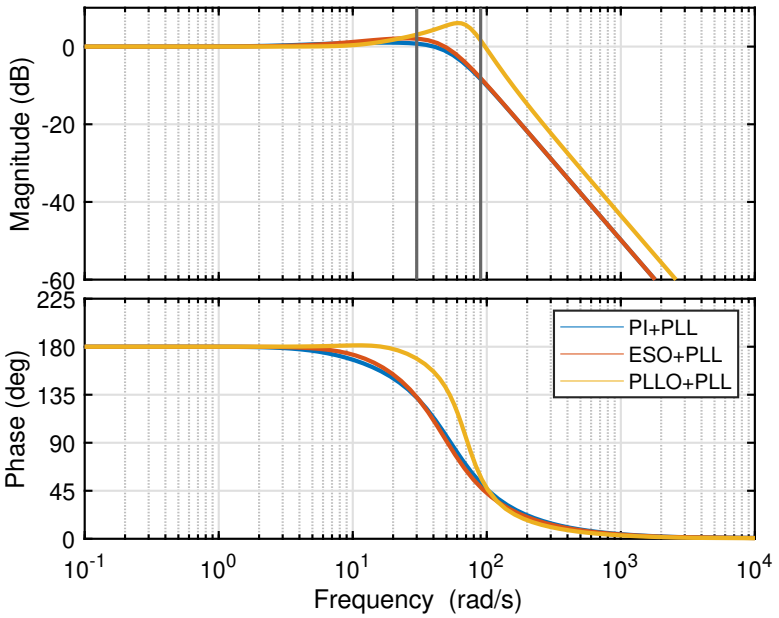

Figure 5.5. *Bode plots for the closed-loop sensorless noise attenuation. Samme y-axis i figur med encoder*

The noise attenuation is also changed due to the velocity PLL. The $PLLO$ has an amplification of the noise in the frequency range of $30 - 90\frac{rad}{s}$. The amplification is higher than without PLL and therefore there is a potential of having more noise during the transient response when using the sensorless feedback compared to the encoder feedback. The ESO and PI controllers have better noise attenuation compared to the $PLLO$, as it was also the case in fig. 3.6 on page 24. The PLL does not amplify the noise significantly for the PI and ESO as it does with the $PLLO$. The noise rejection at the low frequencies are similar between the controllers.

The sensorless drive has been analysed by focusing on implementing the velocity PLL into the ADRC structure, as the velocity PLL proved to be the weakest link in the sensorless drive in chapter 4 on page 29. The analysis shows that the ADRC controllers are stable and able to reject incoming disturbances, but the PLL do change the dynamics of the controllers with the PLL having most impact on the $PLLO$. The sensorless drive is implemented into the experimental setup and tested through the drivecycle.

5.2 Experiments

The same drive cycle as in fig. 3.7 on page 25 is used to test the ADRC controllers performance with sensorless feedback. The parameters for the ADRCs and sensorless drive are the same as in table 3.1 on page 21 and table 4.1 on page 42. The full drivecycle performance can be seen in fig. 5.6 with a zoomed view on the no-load ramp response at $t = 0.35s$.

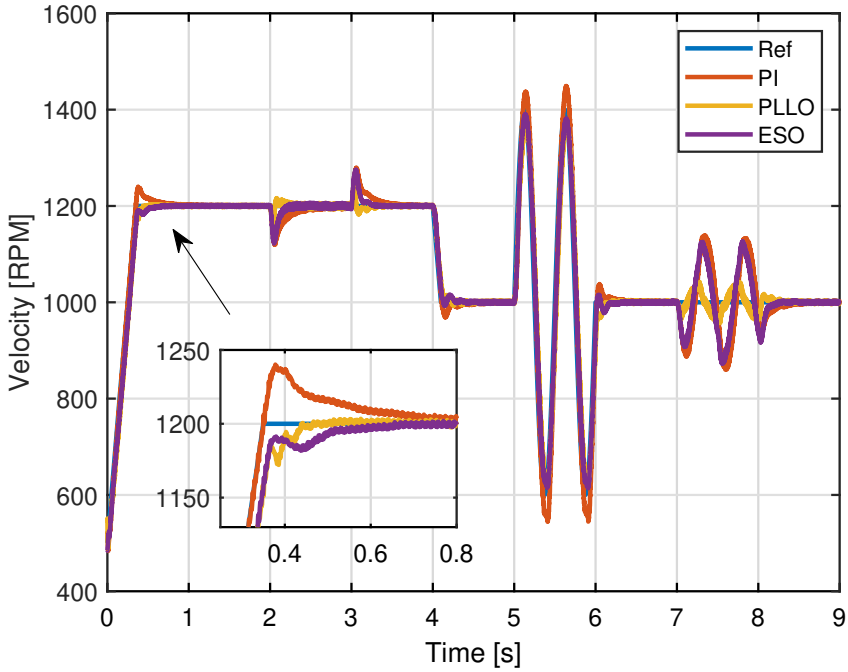

Figure 5.6. *Drivecycle with sensorless feedback and enlarge view of ramp response.*

The drivecycle illustrates that the ADRC with sensorless feedback is capable of running without losing stability. As the ramp reference is met at 1200 RPM it is clear that the transient performance of the ESO and $PLLO$ deviates from the encoder feedback in fig. 3.8 on page 25. Both controllers have oscillations and the settling times remain the same as with encoder feedback, which means the $PLLO$ settles faster than the ESO. The transient oscillations might occur from the lower cut-off frequency of especially the velocity PLL but also the position PLL. As mentioned in the encoder feedback performance at fig. 3.8 on page 25, an inaccurate input parameter b could also degrade the velocity tracking performance, which might be amplified due to the velocity and position PLLs. The PI controller's performance is similar to fig. 4.13 on page 40. In fig. 5.7 on the facing page there is an enlarged graph of the step disturbance rejection in the drivecycle.

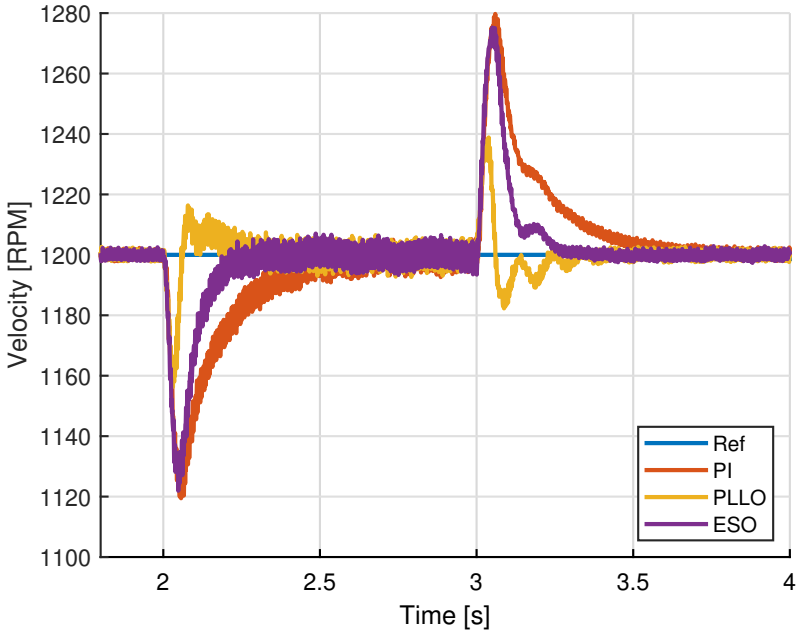

Figure 5.7. *Disturbance rejection with sensorless feedback.*

The ADRC controllers disturbance rejection performances show that the $PLLO$ has the fastest reaction time compared to the ESO and PI. The transient response of the $PLLO$ as the load change occurs and releases at $t = 2s$ and $t = 3s$ respectively, shows that the sensorless drive do change the dynamics in different ways. After the load change occurs at $t = 2s$ and the $PLLO$ overshoots the velocity reference, ripples are disguising the underlying transient dynamics of the $PLLO$, which is more clear when the load is released. These ripples might be related to the position estimation error increases after the load change due to inaccurate inductance L_s, as discussed in section 4.4 on page 36. Too high a position estimation error result in some of the current being placed at the d-axis, which increases ripples from the current controllers. This is likely some of the explanation for the ripples disguising the underlying dynamics at $t \approx 2.1\ s$.
The disturbance rejection oscillations, as the load is released at $t = 3s$, are enlarged compared to the unity step analysis in fig. 5.4 on page 47, which indicates that it is not only the velocity PLL that affects and degrades the performance of the ADRC with sensorless feedback. The extra oscillations that are visible after the load releases indicates that the other factors mentioned earlier, inaccurate input gain b, position estimation error and position PLL at $\omega_{c,pos} = 500\frac{rad}{s}$ do have an impact on the disturbance rejection response. The ESO and PI controllers also have some transient oscillations as the load is released at $t = 3s$, which again indicates more factors than the velocity PLL influences the performance of the controllers. The settling times for the controllers are similar to the encoder feedback in fig. 3.9 on page 26.

The sinus performance of the drive cycle is illustrated in fig. 5.8 on the following page.

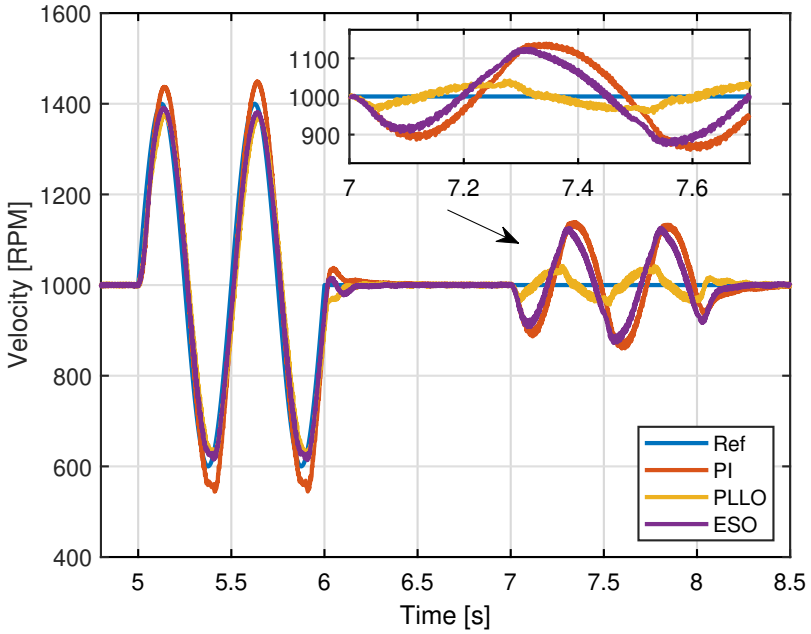

Figure 5.8. *Sinus performance with sensorless feedback.*

The sinus tracking performance of the sensorless drives follow the same tendency as the no-load ramp response, where the PI controller overshoots the reference and the $PLLO$ and ESO have first order responses. This can be seen in the no-load sinus response as the ESO and $PLLO$ do not reach the peak values of the sinus reference, which can only be met by having a faster pole in the first order response as discussed at fig. 3.10 on page 27.
The sinus load rejection performance also have some deviations compared to the encoder feedback in fig. 3.10 on page 27. The $PLLO$'s load rejection is affected by the transient oscillations which visibly can be seen around the velocity peaks in the zoomed view at $t \approx 7.25$ and $t \approx 7.5$. The $PLLO$ is again better at rejecting the load, which is also supported by the bode plot analysis in fig. 5.3 on page 46, as the sinus load input is at 2 Hz. The ESO has better load rejection compared to the PI controller as with encoder feedback. However if the sinus load input is at a higher frequency, e.g. 4 Hz, the bode plot in fig. 5.3 on page 46 indicates the PI controller would have a better load rejection than the ESO. The velocity peaks at the load rejection are also larger compared to fig. 3.10 on page 27, although it is difficult to see visibly from the graphs.

The analysis made in fig. 5.3 on page 46 and fig. 5.4 on page 47 of the disturbance rejection, where the velocity PLL is included in the closed-loop transfer functions, indicated that the performance would degrade when the sensorless control was implemented compared to the encoder feedback. The analysis showed that especially the $PLLO$ would have a performance change by oscillations in the transient response and the experiments supports this initial analysis. The experiments also showed that the performances of the $PLLO$, ESO and PI controllers also were worsened by other factors not included in the analysis. Factors such as the cut-off frequency of the position PLL, the position estimation error and potential inaccurate input b. The direct comparison between analysis and experiment is seen in fig. 5.4 on page 47 were it is obvious at $t = 3s$ that the oscillations in all the controllers are amplified but the settling times remain the same.

5.3 Summery of ADRC with Sensorless Drive

The ADRC with sensorless feedback has been analysed and tested through this chapter. The analysis has been carried out by implementing the velocity PLL into the block diagram of the ADRC control structure in fig. 5.2 on page 44, as the velocity PLL is the limiting factor of the sensorless performance. The disturbance rejection bode diagrams and unity step responses show that the $PLLO$ has transient oscillations by implementing the velocity PLL, whereas the ESO and PI maintains a first order response without transient oscillations. The bode plot analysis in fig. 5.3 on page 46 shows, that the $PLLO$ has some frequencies where the PI and ESO have better load rejection, which is not the case with the encoder feedback as seen in fig. 3.4 on page 22. The drive cycle experiment supported the analysis in fig. 5.4 on page 47 but the oscillations for the $PLLO$ in the experiments are amplified compared to the analysis. Also the ESO and PI controller performances have transient oscillations in fig. 5.7 on page 51, which was not seen in the initial analysis. The same tendencies follow for the velocity reference change in fig. 5.6 on page 50, where the $PLLO$ and ESO have more oscillations compared to the encoder performance in fig. 3.7 on page 25. Despite more transient oscillations occur in the sensorless drive the $PLLO$ has a better load rejection with smaller velocity drop and faster settling time compared to the ESO and PI controllers.

Discussion 6

Through the different chapters of this thesis the main findings have been discussed as they were presented. In this chapter some of the results are further discussed and some possible solutions to the different cases are presented to further improve the performance of the PMSM with ADRC using a sensorless drive.

The ADRC with sensorless feedback in fig. 5.6 on page 50 could perform stable performance through the drive cycle. The experiments showed that the $PLLO$ had the fastest load rejection compared to the ESO and PI controllers, both for the sinusoidal load change of $\pm 10\ Nm$ at $2\ Hz$ in fig. 5.8 on page 52 and the step load change of 5 Nm in fig. 5.7 on page 51. It could be seen in fig. 5.3 on page 46 that some frequencies are better rejected by the PI and ESO compared to the $PLLO$. The step load change showed that the $PLLO$ suffered from transient oscillations, which were not the case with encoder feedback in fig. 3.9 on page 26. The $PLLO$ with sensorless feedback still had a faster settling time after the load change compared to the ESO and PI. Also the velocity drop after the load change was smaller for the $PLLO$ compared to the ESO and PI. The $PLLO$ suffered from greater ripples after the step load change in fig. 5.7 on page 51, which might be due to the position estimation error increases after the load change, as also seen in fig. 4.14 on page 41, and thus the current controllers in the FOC introduces more chattering in the system as they aim for $i_d = 0$. The increased ripples, and thus larger currents, disguises the underlying load rejection dynamics of the $PLLO$ seen after $t = 3s$ in fig. 5.7 on page 51. The ripples also influences the load rejection performance of the ESO and PI as they also have an oscillation in their load rejection performances, which can be seen after $t = 3$ s in fig. 5.7 on page 51, but is not seen after $t = 2\ s$. The steady state ripples are similar for all controllers, which is ± 5 RPM and improving the position estimation error, or lowering the velocity cut-off frequency could possibly improve the steady state- and the transient ripples. The ESO has better performance than the PI controller. This goes for the load rejection and no-load velocity change, where the settling times and velocity drops due to load change are smaller for the ESO compared to the PI. The sinusoidal velocity reference are not met by any of the controllers, where the PI controller overshoots the velocity reference as seen in fig. 5.8 on page 52 due to it has a second order velocity response. The ESO and $PLLO$ controllers have first order responses without overshooting and are lagging the sinusoidal reference.

The experiments through chapter 5 on page 43 were supported by an initial analysis of the velocity PLL being implemented into the block diagram in fig. 5.2 on page 44. The experimental results show that the analysis could be more refined as the $PLLO$, ESO and PI suffered from more transient oscillations than the analysis indicated. The analysis could also have included more of the mentioned parameters that influences the performance. Parameters such as the cutoff frequency of the position PLL and the input gain b could also be included in the closed-loop transfer function analysis in eq. (5.4) on page 44. The position PLL could be included by modifying the PLL term

in eq. (5.4) on page 44 to include both the closed-loop position- and velocity PLL by $PLL_{eq} = PLL_{\omega_m} \cdot PLL_{\theta_e}$. The input gain b could be included by changing the starting equations for the closed-loop transfer function in eq. (5.1) on page 44 and deriving new closed-loop expressions. Different input gains b could be tested to see how an inaccurate parameter b would influence the dynamics of the system. Refining the analysis would give a more accurate estimate of the performance in the experiments, but also increase the complexity of which parameter has the most significant effect on the system.

In the analysis of the ADRC with sensorless control it was seen that just by implementing the PLL into the analytical disturbance resulted in oscillations in the transient disturbance response of the $PLLO$. This could be seen in the closed-loop transfer functions in eq. (5.10) on page 45 that the characteristic equations, and thus the pole placement, would change if the cut-off frequency of the PLL is significant compared to the poles of the system. The cut-off frequency of the PLL is at $\omega_{c,vel} = 100\frac{rad}{s}$ whereas in the LPF with encoder feedback it is at $\omega_{c,LPF} = 628\frac{rad}{s}$. The lower cut-off frequency resulted in later response to load inputs from the IM, which also resulted in transient oscillations. However increasing the PLL cut-off frequency would also increase the steady state ripples, which is harmful to the hardware and mechanical parts of the motor, meaning just increasing the PLL cut-off frequency is not a reliable solution. The encoder LPF can have a higher cut-off frequency due to the encoder calculation of the velocity does not contain as much noise as the back-EMF estimation in the STA-SMO arising from the nature of the sliding mode observer. A way to potentially improve the velocity estimation through the PLL could be to design an adaptive PLL, as in [Wang et al., 2017], that changes with the velocity error between the reference speed ω_m^* and estimated speed $\hat{\omega}_m$ and put an upper cut-off frequency on the velocity error as seen in fig. 6.1.

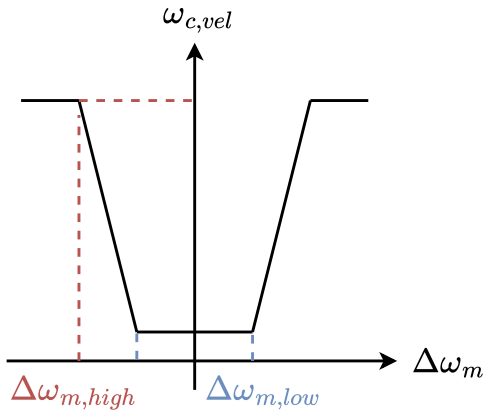

Figure 6.1. *Adaptive PLL based on velocity error* $\Delta\omega_m = \omega_m^* - \hat{\omega}_m$.

This would mean a large velocity error resulted in a higher cut-off frequency in the PLL and thus faster response to an incoming disturbance. This would potentially reduce the oscillations in the transient response as the ADRC would need less peak current to adjust for the load change and have a better imitation of the encoder feedback performance. Then as the velocity error approaches zero the cut-off frequency could be reduced to lower than $\omega_{c,vel} = 100\frac{rad}{s}$, which potentially could minimize steady state ripples as well.

The result of the encoder feedback drivecycle illustrated that there is a difference in the transient response at the initial ramp change at $t = 0.3s$ in fig. 3.8 on page 25

between the $PLLO$ and ESO controller. Theoretically there should not be any difference between their responses as described in section 3.3 on page 19, as they both have a first order response assuming no noise and disturbance. This could indicate that there is an inaccurate control gain $b = \frac{K_t}{J_m}$, which is better compensated in the $PLLO$ than the ESO as the $PLLO$ response resembles better a first order response in fig. 3.8 on page 25 than the ESO. In [Zuo et al., 2019] it is described how an inaccurate input gain b may lead to performance deviations between analytical and experimental performances. The most significant being the inertia J_m, which essentially is an additional gain on the torque constant as J_m is small (<1) in this thesis and divided by the torque constant K_t. Finding a more optimal inertia value could be a solution, but the inertia in a real application where a PMSM might be connected to some drive train with different mechanical parts might need a more sophisticated solution. In [Zuo et al., 2019] an inertia identification is presented as a solution to have a more accurate control gain, which could also be implemented in this thesis to minimise the risk of having an inaccurate inertia parameter.

Through the experiments with sensorless feedback it was seen that more ripples are introduced after a load change as seen in fig. 5.4 on page 47 at $t \approx 2.1$. If this is related to the position estimation error this could be improved in different ways. As described and seen in fig. 4.11 on page 37 and fig. 4.14 on page 41 there are two different factors that may influence the position estimation error; one related to the calculation delay and another related to the load change. If the position estimation error is $-16°$ at steady state after a 10 Nm load change, as in fig. 4.14 on page 41, then the i_q current is reduced to $cos(\frac{-16° \cdot \pi}{180°}) = 0.961$, where the ideal is 1. This means that some of the current is placed at the d-axis for the case in fig. 4.14 on page 41, where the load change is 10 Nm at 1200 RPM, which possibly introduce current ripples in the system.
A solution to the position estimation error related to the calculation delay could simply be to measure the position estimation error at different velocities. Based on the measurements a look up table could be made and compensate the calculation delay at a given motor velocity. This would compensate the DC position estimation error, which in fig. 4.14 on page 41 is $-11°$ at 1200 RPM. This relies on the initial rotor position is the same and a measuring method, which for this thesis, could be done beforehand using the encoder. However in cases where it is not possible to use an encoder beforehand more sophisticated solutions could be implemented as in [Gong et al., 2019], where the calculation delay is estimated from two sampling periods of the phase current. The estimated calculation delay is then used to precompensate the phase current to compensate the position estimation error.
The position estimation error also increases due to load change as seen in fig. 4.14 on page 41, which could be due to inaccurate inductance used in the STA-SMO. The used inductance value is used from the data sheet and not found experimentally, but this could be improved by implementing an online inductance estimator as in [Ye and Yao, 2020], where an SMO estimates the inductance based on a flux observer. However estimating the inductance and changing it dynamically also means that other parts of the motor control must be changed dynamically. As an example if the inductance parameter is changed the observer gains k_1 and k_2 of the STA-SMO in eq. (4.15) on page 33 might also need to be changed as k_i are found iterative based on the initial inductance. This means that some relation between the inductance and observer gains must be established in order to secure stability if the inductance is changed by an online observer.

Conclusion 7

The purpose of this thesis was to investigate how a PMSM could be controlled by an ADRC in sensored and sensorless conditions. The sensorless control was based on back-EMF estimation for rotor position estimation by a STA-SMO and filtered through PLLs for both position- and velocity estimation. The ADRC was analysed through closed-loop transfer functions, simulated and tested in an experimental setup and the ADRC's performances were compared to traditional PI velocity control.
The ADRC was based on an disturbance observer that estimated both the internal- and external disturbances into a total disturbance. Initially the two different ADRCs, the $PLLO$ and ESO, were analysed and tested with an encoder feedback and it can be concluded through analysis and experiments that the $PLLO$ have a better load rejection compared to the ESO and PI controller. The analysis showed that the $PLLO$ had a load rejection of 40 $\frac{dB}{dec}$ compared to the ESO and PI controllers 20 $\frac{dB}{dec}$. This meant that the velocity drop was lower and settling time faster for the $PLLO$, as a load change occurred, compared to the ESO and PI. It can also be concluded the ESO had a better load rejection and faster tracking settling time compared to the PI controller. This was due to the estimated disturbance of the ESO, based on the integral output of the observer PI, had faster load rejection properties than the integration term of the traditional PI controller. It can be concluded the ESO and $PLLO$ had a first order tracking response, which meant the tracking response did not overshoot as the PI controller. It can also be concluded that none of the controllers were able to follow the sinusoidal velocity reference, as their poles were not fast enough to follow a sinus velocity reference of 2 Hz.

The sensorless drive was able to estimate the back-EMF and thus estimating the rotor position. It can be concluded that the STA-SMO could run the PMSM with some performance deviations compared to the PI controller with encoder feedback. The velocity drop were larger as load change occurred and the overshoot was higher for a reference velocity change compared to the encoder feedback. The settling times remained the same for the encoder- and sensorless feedback. It can be concluded that the most significant component that degraded the performance was the cutoff frequency of the velocity PLL. The lower cutoff frequency of $100\frac{rad}{s}$ compared to the encoder LPF at $628\frac{rad}{s}$ meant that the estimated velocity was slower to respond to inputs being changed.

The ADRC controllers were also tested with the sensorless control. It can be concluded that the $PLLO$ still performed best with sensorless feedback as it had faster load rejection and faster tracking settling time compared to the ESO and PI. However it can also be concluded that the transient performance of the $PLLO$ suffered from oscillations due to the implementation of the sensorless drive. The oscillations were also seen in the ESO and PI controllers, but not as significant as with the $PLLO$. This change in transient response for the $PLLO$ was also supported by the analysis, where the velocity PLL was implemented into the controllers closed-loop transfer functions. It can be concluded that the analysis could be more refined by implementing more parameters into the analysis, such as the position PLL, inaccurate input gain b and the position estimation error.

Bibliography

Fitzgerald og Kingsley, **2014**. A.E. Fitzgerald and Charles Kingsley. *Electric Machinery*. ISBN: 0073380466, Paperback McGraw Hill, 2014.

Gong et al., **2019**. Chao Gong, Yihua Hu, Jinqiu Gao, Yangang Wang and Liming Yan. *An improved delay-suppressed sliding-mode observer for sensorless vector-controlled PMSM*. IEEE Transactions on Industrial Electronics, 67(7), 5913–5923, 2019.

Guo et al., **2017**. Guo, Baoling, Bacha, Seddik and Mazen Alamir. *A review on ADRC based PMSM control designs*. IECON 2017 - 43rd Annual Conference of the IEEE Industrial Electronics Society, pages 1747–1753, 2017. doi: 10.1109/IECON.2017.8216296.

Jung et al., **2015**. Jin-Woo Jung, Viet Quoc Leu, Ton Duc Do, Eun-Kyung Kim and Han Ho Choi. *Adaptive PID Speed Control Design for Permanent Magnet Synchronous Motor Drives*. IEEE Transactions on Power Electronics, 30(2), 900–908, 2015. doi: 10.1109/TPEL.2014.2311462.

Li et al., **2023**. Shuai Li, Hai Wang, Chunlai Yang, Henian Li, Jinsong Gui and Ronghua Fu and. *Current decoupling control of permanent magnet synchronous motor based on improved nonlinear extended state observer*. Journal of Vibration and Control, 0, 1–17, 2023. doi: 10.1177/10775463231222780.

Liang et al., **2017a**. Donglai Liang, Jian Li and Ronghai Qu. *Sensorless Control of Permanent Magnet Synchronous Machine Based on Second-Order Sliding-Mode Observer With Online Resistance Estimation*. IEEE TRANSACTIONS ON INDUSTRY APPLICATIONS, 53, 3672–3682, 2017a. doi: 10.1109/TIA.2017.2690218.

Liang et al., **2017b**. Donglai Liang, Jian Li, Ronghai Qu and Wubin Kong. *Adaptive Second-Order Sliding-Mode Observer for PMSM Sensorless Control Considering VSI Nonlinearity*. IEEE TRANSACTIONS ON POWER ELECTRONICS, 33, 8994–9004, 2017b. doi: 10.1109/TPEL.2017.2783920.

Qiao et al., **2013**. Zhaowei Qiao, Tingna Shi, Yindong Wang, Yan Yan, Changliang Xia and Xiangning He. *New Sliding-Mode Observer for Position Sensorless Control of Permanent-Magnet Synchronous Motor*. IEEE Transactions on Industrial Electronics, 60, 710–719, 2013.

SCANCON, **2015**. SCANCON. *Type SCA50*. `https://www.scancon.dk/media/1194/sca50-specifications-17.pdf`, 2015. Last visit: 08-09-2024.

Shtessel et al., **2014**. Yuri Shtessel, Christopher Edwards, Leonid Fridman and Arie Levant. *Sliding Mode Control and Observation*. ISBN: 978-1-4899-9122-5, Paperback Birkhäuser New York, NY, 2014.

Siemens, **2005**. Siemens. *Configuration manual 10/2005 edition*. `https://cache.industry.siemens.com/dl/files/289/28708289/att_2592/v1/PFT6_1005_en.pdf`, 2005. Last visit: 08-09-2024.

Utkin, **2011**. Vadim Utkin. *Chattering Problem*. IFAC Proceedings Volumes, 44, 13374–13379, 2011. doi: 10.3182/20110828-6-IT-1002.00587.

Wang et al., **2017**. Dong Wang, Kaiyuan Lu, Peter Omand Rasmussen and Zhenyu Yang. *Comparative Study of Low-Pass Filter and Phase-Locked Loop Type Speed Filters for Sensorless Control of AC Drives*. CES TRANSACTIONS ON ELECTRICAL MACHINES AND SYSTEMS, 1, 207–215, 2017. doi: 10.23919/TEMS.2017.7961343.

Wang et al., **2012**. Zihui Wang, Kaiyuan Lu and Frede Blaabjerg. *A Simple Startup Strategy Based on Current Regulation for Back-EMF-Based Sensorless Control of PMSM*. IEEE Transactions on Power Electronics, 27(8), 3817–3825, 2012. doi: 10.1109/TPEL.2012.2186464.

Wilson et al., **2010**. Simon Delamere Wilson, Paul Stewart and Benjamin P. Taylor. *Methods of Resistance Estimation in Permanent Magnet Synchronous Motors for Real-Time Thermal Management*. IEEE Transactions on Energy Conversion, 25(3), 698–707, 2010. doi: 10.1109/TEC.2010.2051811.

Ye og Yao, **2020**. Shuaichen Ye and Xiaoxian Yao. *A Modified Flux Sliding-Mode Observer for the Sensorless Control of PMSMs With Online Stator Resistance and Inductance Estimation*. IEEE Transactions on Power Electronics, 35(8), 8652–8662, 2020. doi: 10.1109/TPEL.2019.2963112.

Yong et al., **2023**. Li Yong, Hu Han and Shi Peicheng. *A Review of Position Sensorless Compound Control for PMSM Drives*. World Electric Vehicle Journal, 14 (2), 11352–11367, 2023. doi: DOI:10.3390/wevj14020034.

Zuo et al., **2023**. Ying Zuo, Chunyan Lai and K. Lakshmi Varaha Iyer. *A Review of Sliding Mode Observer Based Sensorless Control Methods for PMSM Drive*. IEEE Transactions on Power Electronics, 38(9), 11352–11367, 2023. doi: 10.1109/TPEL.2023.3287828.

Zuo et al., **2019**. Yuefei Zuo, Xiaoyong Zhu, Li Quan, Chao Zhang, Yi Du and Zixuan Xiang. *Active Disturbance Rejection Controller for Speed Control of Electrical Drives Using Phase-Locking Loop Observer*. IEEE TRANSACTIONS ON INDUSTRIAL ELECTRONICS, 66, 1748–1759, 2019. doi: 10.1109/TIE.2018.2838067.

Friction Test A

The friction parameters are determined experimentally by running the PMSM at constant velocities and without load changes, leaving the equation of motion in eq. (2.10) on page 9 into eq. (A.1). A constant velocity means the acceleration is $\dot{\omega}_m(t) = 0$ and no load means $\tau_L(t) = 0$.

$$0 = \tau_e(t) - \tau_f(t) \tag{A.1}$$

This means the input torque is equal to the friction torque, and running at different steady state velocities results in a linear relation where the friction changes linearly with changing velocities. The linear relation can be seen in fig. A.1 and the viscous friction term is $B_v = 0.0014\ \frac{Nm \cdot s}{rad}$ and the intersection with the y-axis is the static Coulomb friction $C = 0.2429\ Nm$. The test is performed in the positive direction and it is assumed running the PMSM in the opposite direction would result in the same values of B_v and C.

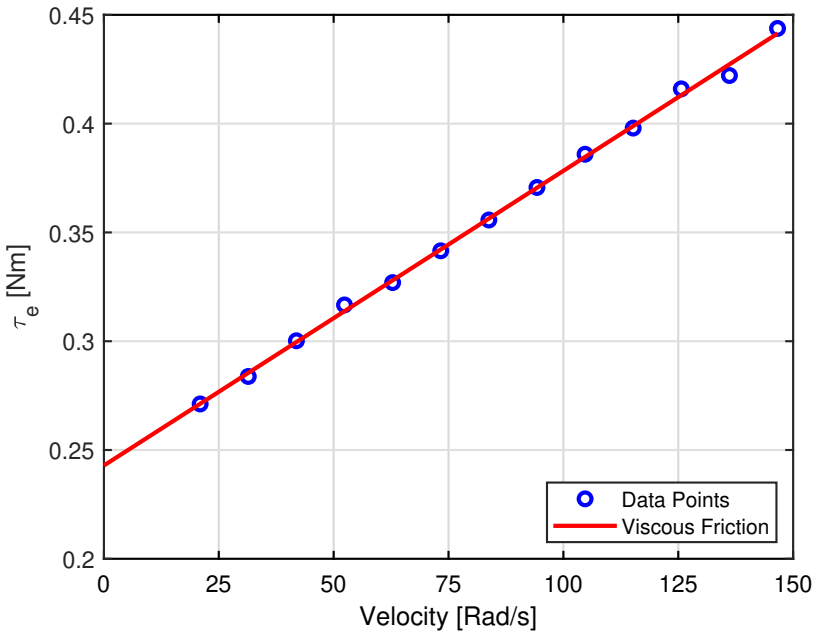

Figure A.1. *Electromagnetic torque vs. mechanical speed.*

Closed-Loop Derivations B

The transfer functions used in the ADRC controller analysis in chapter 3 on page 15 are derived in this appendix.

PI Transfer Functions

The PI transfer function for the reference velocity is found from fig. 3.3 on page 18, where the disturbance and noise are equal to zero. Closing the loop results in the following transfer function.

$$\frac{\omega_m}{\omega_m^*} = \frac{k_{ps} + \frac{k_{is}}{s}}{1 + k_{ps} + \frac{k_{is}}{s}} \tag{B.1}$$

$$\frac{\omega_m}{\omega_m^*} = \frac{k_{ps}s + k_{is}}{s^2 + k_{ps} + k_{is}} \tag{B.2}$$

The disturbance closed loop transfer function is similarly found by letting the noise and velocity reference equal zero.

$$\frac{\omega_m}{d} = \frac{\frac{1}{s}}{1 + (k_{ps} + \frac{k_{is}}{s})\frac{1}{s}} \tag{B.3}$$

$$\frac{\omega_m}{d} = \frac{s}{s^2 + k_{ps}s + k_{is}} \tag{B.4}$$

The noise closed-loop transfer function is found by taking the reference velocity and disturbance to be equal zero.

$$\omega_m = -(\omega_m + \delta)(k_{ps} + \frac{k_{is}}{s})\frac{1}{s} \tag{B.5}$$

$$\omega_m(1 + \frac{k_{ps+k_{is}}}{s^2} = -\delta\frac{k_{ps}s + k_{is}}{s^2} \tag{B.6}$$

$$\frac{\omega_m}{\delta} = -\frac{k_{ps}s + k_{is}}{s^2 + k_{ps}s + k_{is}} \tag{B.7}$$

PLLO Transfer Functions

The reference velocity transfer function is derived by looking at fig. 3.2 on page 17 and assuming the disturbance- and noise inputs are equal to zero. This means the observer part can be neglected and the velocity reference transfer function is similar for the $PLLO$ and ESO controllers. This results in the closed-loop transfer function in eq. (B.9)

$$\frac{\omega_m}{\omega_m^*} = \frac{\frac{k_{ps}}{s}}{1 + \frac{k_{ps}}{s}} \tag{B.8}$$

$$\frac{\omega_m}{\omega_m^*} = \frac{k_{ps}}{s + k_{ps}} \tag{B.9}$$

The disturbance transfer function of the $PLLO$ is derived by assuming the input reference and the noise being zero. This results in an equivalent block diagram as in fig. B.1, where the switch S_1 is connected to the $PLLO$ connection.

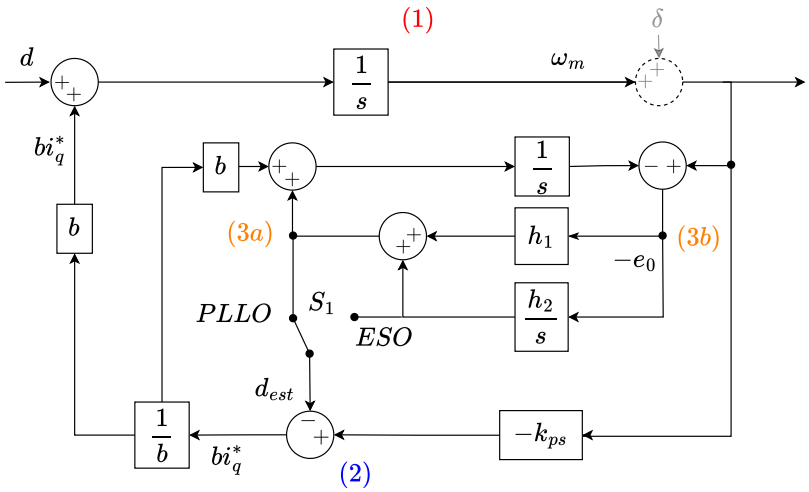

Figure B.1. *Block diagram of PLLO with* $\omega_m^*(t) = 0$ *and* $\delta(t) = 0$.

Three equations are made to derive the disturbance transfer function of the ADRC. The equations for the $PLLO$ are derived based on the red point (1), blue point (2) and orange point (3a) and seen in eq. (B.10), (B.11) and (B.12)

$$(1) \quad \frac{1}{s}(d + bi_q^*) = \omega_m \tag{B.10}$$

$$(2) \quad -k_{ps}\omega_m - d_{est} = bi_q^* \tag{B.11}$$

$$(3a) \quad [\omega_m - \frac{1}{s}(bi_q^* + d_{est})](h_1 + \frac{h_2}{s}) = d_{est} \tag{B.12}$$

The equation for point (2) can be rewritten by isolating d_{est} as in eq. (B.13), and the equation for point (3a) can be rewritten as in eq. (B.14).

$$d_{est} = -k_{ps}\omega_m - bi_q^* \tag{B.13}$$

$$s\omega_m - bi_q^* = (\frac{s^2}{sh_1 + h_2} + 1)d_{est} \tag{B.14}$$

Then eq. (B.13) can be substituted into eq. (B.14) and results in eq. (B.15)

$$-s\omega_m = (\frac{s^2}{sh_1 + h_2} + 1)k_{ps}\omega_m + (\frac{s^2}{sh_1 + h_2})bi_q^* \tag{B.15}$$

And rearranging the expression such that ω_m and bi_q^* are isolated at each site of the equation results in eq. (B.16).

$$\underbrace{-(\frac{k_{ps}s^2}{sh_1 + h_2} + k_{ps} + s)}_{A}\omega_m = \underbrace{(\frac{s^2}{sh_1 + h_2})}_{B} bi_q^* \tag{B.16}$$

Then the expression of bi_q^* can be rewritten from eq. (B.10) on the facing page into eq. (B.17).

$$bi_q^* = s\omega_m - d \tag{B.17}$$

And inserting eq. (B.17) into eq. (B.16).

$$A\omega_m = Bs\omega_m - Bd \tag{B.18}$$

Now the transfer function can be expressed in terms of $\frac{\omega_m}{d}$ as in eq. (B.19).

$$\frac{\omega_m}{d} = \frac{B}{Bs - A} \tag{B.19}$$

Inserting the expressions of A and B in the underbraces in eq. (B.16) results in the disturbance closed loop transfer function.

$$\frac{\omega_m}{d} = \frac{s^2}{(s^2 + h_1 s + h_2)(k_{ps} + s)} \tag{B.20}$$

Noise Transfer Function

The noise transfer function $\frac{\omega_m}{\delta}$ can also be found from fig. B.1 on the facing page and setting $d = 0$ and leeting the input come from δ. This means the three equation points are changed into eq. (B.21), (B.22) and (B.23)

$$(1) \quad \frac{1}{s}bi_q^* = \omega_m \tag{B.21}$$

$$(2) \quad -k_{ps}(\omega_m + \delta) - d_{est} = bi_q^* \tag{B.22}$$

$$(3a) \quad [(\omega_m + \delta) - \frac{1}{s}(bi_q^* + d_{est})](h_1 + \frac{h_2}{s}) = d_{est} \tag{B.23}$$

Then following the derivations for disturbance with the new equation formulations result in a closed loop noise transfer function as in eq. (B.24) on the following page

$$\frac{\omega_m}{\delta} = -\frac{(h_1 k_{ps} s + h_1 s^2 + k_{ps} s^2 + h_2 k_{ps} + h_2 s)}{(s^2 + h_1 s + h_2)(s + k_{ps})} \tag{B.24}$$

The closed loop equation can be simplified as the nominator contains the same components as the denominator if the parentheses are expanded except s^3. Therefore it can be simplified as in eq. (B.25)

$$\frac{\omega_m}{\delta} = \frac{s^3}{(s^2 + h_1 s + h_2)(s + k_{ps})} - 1 \tag{B.25}$$

ESO Transfer Functions

The reference velocity transfer function of the *ESO* is similar to the *PLLO* in eq. (B.9) on page 62. The disturbance transfer function can similarly as the *PLLO* be derived based on fig. B.1 on page 62, where the switch, S_1, is connected to *ESO*. To derive the transfer function the equations of the block diagram is again divided into three parts and point (1), (2) and (3b) are given by eq. (B.26), (B.27) and (B.28).

$$(1) \quad \frac{1}{s}(d + bi_q^*) = \omega_m \tag{B.26}$$

$$(2) \quad -k_{ps}\omega_m - (-e_0)(h_1 + \frac{h_2}{s}) = bi_q^* \tag{B.27}$$

$$(3b) \quad \omega_m - \frac{1}{s}(bi_q^* + (-e_0)(h_1 + \frac{h_2}{s})) = -e_0 \tag{B.28}$$

The equation for point (2) can be rewritten by isolating $-e_0$ as in eq. (B.29), and the equation for point (3b) can be rewritten as in eq. (B.30).

$$-e_0 = \frac{s}{h_2}(-k_{ps}\omega_m - bi_q^*) \tag{B.29}$$

$$\omega_m - \frac{1}{s}bi_q^* = (1 + \frac{sh_1 + h_2}{s^2})(-e_0) \tag{B.30}$$

Then eq. (B.29) can be substituted into eq. (B.30) and results in eq. (B.31)

$$\omega_m - \frac{1}{s}bi_q^* = (\frac{s^2 + sh_1 + h_2}{h_2 s})(-k_{ps}\omega_m - bi_q^*) \tag{B.31}$$

And rearranging the expression such that ω_m and bi_q^* are isolated at each site of the equation results in eq. (B.32).

$$\underbrace{(1 + k_{ps}(\frac{s^2 + sh_1 + h_2}{h_2 s}))}_{A}\,\omega_m = \underbrace{-(\frac{s^2 + h_1 s}{h_2 s})}_{B}\,bi_q^* \tag{B.32}$$

Then the expression of bi_q^* can be rewritten from eq. (B.26) into eq. (B.33) on the facing page.

$$bi_q^* = s\omega_m - d \tag{B.33}$$

And inserting eq. (B.33) into eq. (B.32) on the facing page.

$$A\omega_m = Bs\omega_m - Bd \tag{B.34}$$

Now the transfer function can be expressed in terms of $\frac{\omega_m}{d}$ as in eq. (B.35).

$$\frac{\omega_m}{d} = \frac{B}{Bs - A} \tag{B.35}$$

Inserting the expressions of A and B in the underbraces in eq. (B.32) on the facing page results in the disturbance closed loop transfer function.

$$\frac{\omega_m}{d} = \frac{s(s + h_1)}{(s^2 + h_1 s + h_2)(k_{ps} + s)} \tag{B.36}$$

Noise Transfer Function

The noise closed loop transfer function can similarly be found as the $PLLO$ by letting $d = 0$ and δ be the input in fig. B.1 on page 62. Again the equations for point (1), (2) and (3b) are augmented and results in eq. (B.37), (B.38) and (B.39).

$$(1) \quad \frac{1}{s} b i_q^* = \omega_m \tag{B.37}$$

$$(2) \quad -k_{ps}(\omega_m + \delta) - (-e_0)(h_1 + \frac{h_2}{s}) = b i_q^* \tag{B.38}$$

$$(3b) \quad (\omega_m + \delta) - \frac{1}{s}(b i_q^* + (-e_0)(h_1 + \frac{h_2}{s})) = -e_0 \tag{B.39}$$

Then the closed loop noise transfer function can be found by going through the derivation process with the new equations. This results in the noise closed loop transfer function in eq. (B.40), which is simplified as the $PLLO$ expression in eq. (B.25) on the facing page.

$$\frac{\omega_m}{\delta} = \frac{s^2(s + h1)}{(s^2 + h_1 s + h_2)(s + k_{ps})} - 1 \tag{B.40}$$

STA Stability C

A stability analysis of the conventional SMO for back-EMF estimation is derived through this appendix. The stability analysis is based on sliding mode theory from [Shtessel et al., 2014] and back-EMF SMO in [Qiao et al., 2013].

The SMO is based on the stator voltage equations of the SMO in the $\alpha\beta$-frame as shown in eq. (C.1)

$$\begin{aligned} \frac{d}{dt}i_\alpha(t) &= \frac{1}{L_s}(-Ri_\alpha(t) + u_\alpha(t) - e_\alpha(t)) \\ \frac{d}{dt}i_\beta(t) &= \frac{1}{L_s}(-Ri_\beta(t) + u_\beta(t) - e_\beta(t)) \end{aligned} \tag{C.1}$$

The sliding surface is defined as in eq. (4.8) on page 31 and rewritten in eq. (C.2), where $\hat{i}_s(t)$ is the estimated $\alpha\beta$ currents $\hat{i}_s(t) = [\hat{i}_\alpha(t) \;\; \hat{i}_\beta(t)]^T$ and $i_s(t)$ is the measured current $i_s(t) = [i_\alpha(t) \;\; i_\beta(t)]^T$.

$$S(t, X) = \hat{i}_s(t) - i_s(t) = \bar{i}_s(t) \tag{C.2}$$

Then the back-EMF terms $e_\alpha(t)$ and $e_\beta(t)$ in eq. (C.1) are replaced with a switching function as in eq. (C.3), and inserted into eq. (C.1) resulting in the SMO in eq. (C.4). The switching function F is a *sign* function in the conventional SMO and k is the observer gain.

$$\hat{e}_{\alpha\beta}(t) = kF(\hat{i}_{\alpha\beta}(t) - i_{\alpha\beta}(t)) \tag{C.3}$$

$$\begin{aligned} \frac{d}{dt}\hat{i}_\alpha(t) &= \frac{1}{L_s}(-R\hat{i}_\alpha(t) + u_\alpha(t) - ksign(\hat{i}_\alpha(t) - i_\alpha(t))) \\ \frac{d}{dt}\hat{i}_\beta(t) &= \frac{1}{L_s}(-R\hat{i}_\beta(t) + u_\beta(t) - ksign(\hat{i}_\beta(t) - i_\beta(t))) \end{aligned} \tag{C.4}$$

To verify the stability of the SMO a Lyapunov candidate function, $V(t, X)$, must be positive definite and its derivative negative semi-definite. This is tested with the Lyapunov candidate function in eq. (C.5).

$$V(t, X) = \frac{1}{2}S(t, X)^T S(t, X) \tag{C.5}$$

This function is positive definite and its derivative must be negative semi-definite to ensure the observer is asymptotic stable as seen in eq. (C.6).

$$\dot{V}(t, X) = S(t, X)^T \dot{S}(t, X) \quad \leq \quad 0. \tag{C.6}$$

Then error equations are made by subtracting eq. (C.1) on the facing page from eq. (C.4) on the preceding page, which results in eq. (C.7)

$$\begin{aligned}\frac{d}{dt}S_\alpha(t,X) &= \frac{1}{L_s}(-RS_\alpha(t,X) + e_\alpha(t) - ksign(\hat{i}_\alpha(t) - i_\alpha(t))) \\ \frac{d}{dt}S_\beta(t,X) &= \frac{1}{L_s}(-RS_\beta(t,X) + e_\beta(t) - ksign(\hat{i}_\beta(t) - i_\beta(t)))\end{aligned} \tag{C.7}$$

Where $S_\alpha(t,X) = [\hat{i}_\alpha(t) - i_\alpha(t)]$ and $S_\beta(t,X) = [\hat{i}_\beta(t) - i_\beta(t)]$. Now the error equations in eq. (C.7) can be inserted into the Lyapunov derivative function in eq. (C.6) on the facing page, which results in eq. (C.8).

$$\begin{aligned}\dot{V}(t,x) &= S(t,X)^T\dot{S}(t,X) = S_\alpha(t,X)\dot{S}_\alpha(t,X) + S_\beta(t,X)\dot{S}_\beta(t,X) \\ \dot{V}(t,x) &= \frac{1}{L_s}[\underbrace{(\hat{i}_\alpha(t) - i_\alpha(t))e_\alpha(t)}_{Positive\ term} - k(\hat{i}_\alpha(t) - i_\alpha(t))sign(\hat{i}_\alpha(t) - i_\alpha(t))] \\ &\quad + \frac{1}{L_s}[\underbrace{(\hat{i}_\beta(t) - i_\beta(t))e_\beta(t)}_{Positive\ term} - k(\hat{i}_\beta(t) - i_\beta(t))sign(\hat{i}_\beta(t) - i_\beta(t))] \\ &\quad - \frac{R}{L_s}[(\hat{i}_\alpha(t) - i_\alpha(t))^2 + (\hat{i}_\beta(t) - i_\beta(t))^2]\end{aligned} \tag{C.8}$$

To ensure eq. (C.8) is ≤ 0 the positive terms must be smaller than the negative terms of the equations. The only adjustable parameter is the observer gain k, which is multiplied the same term, $\hat{i}_{\alpha\beta}(t) - i_{\alpha\beta(t)}$, as $e_{\alpha\beta}(t)$. This means a relation can be put up to ensure stability of the SMO as in eq. (C.9).

$$k \geq max(|e_\alpha||e_\beta|) \tag{C.9}$$

When the criteria in eq. (C.9) is met the observer is globally asymptotically stable as the derivative of the Lyapunov function in eq. (C.8) is negative definite.